

Sparse-View X-Ray CT Reconstruction Using ℓ_1 Prior with Learned Transform

Xuehang Zheng[†], Il Yong Chun[†], *Member, IEEE*, Zhipeng Li, *Student Member*,
Yong Long, *Member, IEEE*, and Jeffrey A. Fessler, *Fellow, IEEE*

Abstract—A major challenge in X-ray computed tomography (CT) is reducing radiation dose while maintaining high quality of reconstructed images. To reduce the radiation dose, one can reduce the number of projection views (sparse-view CT); however, it becomes difficult to achieve high-quality image reconstruction as the number of projection views decreases. Researchers have applied the concept of learning sparse representations from (high-quality) CT image dataset to the sparse-view CT reconstruction. We propose a new statistical CT reconstruction model that combines penalized weighted-least squares (PWLS) and ℓ_1 prior with learned sparsifying transform (PWLS-ST- ℓ_1), and a corresponding efficient algorithm based on Alternating Direction Method of Multipliers (ADMM). To moderate the difficulty of tuning ADMM parameters, we propose a new ADMM parameter selection scheme based on approximated condition numbers. We interpret the proposed model by analyzing the minimum mean square error of its (ℓ_2 -norm relaxed) image update estimator. Our results with the extended cardiac-torso (XCAT) phantom data and clinical chest data show that, for sparse-view 2D fan-beam CT and 3D axial cone-beam CT, PWLS-ST- ℓ_1 improves the quality of reconstructed images compared to the CT reconstruction methods using edge-preserving regularizer and ℓ_2 prior with learned ST. These results also show that, for sparse-view 2D fan-beam CT, PWLS-ST- ℓ_1 achieves comparable or better image quality and requires much shorter runtime than PWLS-DL using a learned overcomplete dictionary. Our results with clinical chest data show that, methods using the unsupervised learned prior generalize better than a state-of-the-art deep “denoising” neural network that does not use a physical imaging model.

Index Terms—Sparse-view CT, Model-based image reconstruction, Machine learning, Dictionary learning, Transform learning, Sparse representations, ℓ_1 -norm regularization, Minimum mean square error analysis.

I. INTRODUCTION

Radiation dose reduction is a major challenge in X-ray computed tomography (CT). Sparse-view CT reduces dose by acquiring fewer projection views [1], [2]. However, as the number of projection views decreases, it becomes harder to achieve high quality (high resolution, contrast, and signal-to-noise ratio) image reconstruction. Inspired by compressed sensing theories exploiting sparsity of signals [3]–[5], there

have been many studies of sparse-view CT reconstruction with total variation [6]–[10] or other sparsity promoting regularizers [1], [2].

Researchers have applied (deep) neural networks (NNs) to sparse-view and low-dose CT reconstruction problems. Early works focused on image denoising [11]–[15] using the good mapping capabilities of deep NNs. However, the greater mapping capability can increase the chance of causing some artificial features when test images are not similar to training images. (See Fig. 6.) More recent works combined image mapping NNs with model-based image reconstruction (MBIR) frameworks that consider CT physics [16]–[20]. However, for *general* image mapping NNs, it is difficult to explicitly write the corresponding optimization problems within an MBIR framework. Without explicit cost functions, it is challenging to guarantee the non-expansiveness (or 1-Lipschitz continuity) of the image mapping NNs and obtain “optimal” and convergent image reconstruction, especially when the mapping NNs are identical across iterations [19]. In addition, considering that the methods are trained with supervised learning, one would expect optimal results by using pairs of “noiseless” and “noisy” images in the training processes. In practice, however, it is challenging to obtain noiseless images to construct such paired training dataset in CT imaging. Based on a recent “Noise2Noise” training method [21], some recent works [22], [23] show that training image mapping NNs with pairs of noisy images could provide satisfactory image quality in certain applications. However, training with noisy images has certain limitations in sparse-view CT reconstruction (see Section S.I in the supplement).

Alternatively, researchers have learned prior information in an unsupervised way by using (unpaired) datasets that consist of high-quality images, and exploited it for solving inverse problems [24]–[36]. This unsupervised framework can resolve the aforementioned issues of the supervised framework. The corresponding learned operators sparsify a specific set of training images, but have the potential to represent a broader range of test images compared to the supervised image mapping NNs. (See Fig. 6.) In addition, one can explicitly formulate an optimization problem for image recovery using the learned sparsifying operators. Particularly, in MBIR algorithms, the authors in [19] show that the learned convolutional analysis operator using tight-frame (TF) filters [24] becomes a non-expansive image mapping autoencoder (of encoding convolution, nonlinear thresholding, and decoding convolution [24]). The unsupervised framework has been widely applied in image denoising problems and provided

[†]These two authors contributed equally to this work.

This work is supported in part by the National Natural Science Foundation of China under Grant 61501292, and in part by the NIH under Grant U01 EB018753. (Corresponding author: Yong Long.)

Xuehang Zheng, Zhipeng Li and Yong Long are with the University of Michigan - Shanghai Jiao Tong University Joint Institute, Shanghai Jiao Tong University, Shanghai 200240, China (email: {zhxhang, zhipengli, yong.long}@sjtu.edu.cn).

Il Yong Chun and Jeffrey A. Fessler are with the Department of Electrical Engineering and Computer Science, The University of Michigan, Ann Arbor, MI 48019 USA (email: {iyochun, fessler}@umich.edu).

promising results [26]–[30]. Recently, patch-based sparsifying operator learning frameworks [28]–[30] have been successfully applied to improve low-dose CT reconstruction [31]–[36]. The authors in [36] reported that a union of transforms learned via clustering different features can further improve image quality of reconstructions over the low-dose CT reconstruction method using a (square) sparsifying transform (ST) [34]. In some computer vision applications, the studies [37], [38] show that robust dictionary learning incorporating ℓ_1 prior outperforms that using ℓ_2 prior when outliers exist.

This paper was inspired by a simple observation related to our recent study [34]: for the penalized weighted-least squares (PWLS) reconstruction method using ℓ_2 prior with a learned ST (PWLS-ST- ℓ_2) [34], the sparsification error histograms match a Laplace distribution over the iterations; see Fig. 1. The question then arises, “Does the learned prior experience model mismatch in testing stage?” To answer this question, we aim to investigate learned STs for regularization. This paper

- 1) proposes a new MBIR model that combines PWLS and ℓ_1 prior with learned ST (PWLS-ST- ℓ_1),
- 2) develops a corresponding efficient algorithm based on Alternating Direction Method of Multipliers (ADMM) [39] with a new ADMM parameter selection scheme based on approximated condition numbers,
- 3) and interprets the proposed model by analyzing the empirical mean square error (MSE) of its image update estimator, and the minimum mean square error (MMSE) of its ℓ_2 -norm relaxed image update estimator.

Our results with the extended cardiac-torso (XCAT) phantom data [40] and clinical chest data show that, for sparse-view 2D fan-beam CT and 3D axial cone-beam CT, PWLS-ST- ℓ_1 improves the reconstruction quality compared to a PWLS reconstruction method with an edge-preserving regularizer (PWLS-EP), and PWLS-ST- ℓ_2 . These results also show that, for sparse-view 2D fan-beam CT, PWLS-ST- ℓ_1 achieves comparable or better image quality and requires much shorter runtime than PWLS-DL using a learned overcomplete dictionary. Our results with clinical chest data show that, MBIR methods using the learned prior in an unsupervisedly fashion generalize better than FBPCNN [14], a state-of-the-art deep “denoising” neural network.

For sparse-view CT application, a similar approach that uses ℓ_1 prior with a dictionary was introduced in [33]; however, there are three major differences. First, we focus on an *analysis* approach (e.g., transform and convolutional analysis operator [24]), whereas [33] is based on a *synthesis* perspective (e.g., dictionary and convolutional dictionary [26]). Second, we pre-learn our signal model in an unsupervised way and exploit it in CT MBIR as a prior, whereas [33] adaptively estimates the dictionary in reconstruction. Because their dictionary changes during reconstruction, their main concern is not related to the model mismatch. Third, we directly solve the ℓ_1 minimization via ADMM, whereas [33] uses a reweighted- ℓ_2 minimization framework. Our previous conference paper [41] presented a brief study of the proposed PWLS-ST- ℓ_1 model for sparse-view 2D fan-beam CT scans with XCAT phantom. This paper extends our previous work to 3D axial cone-beam CT,

describes and investigates our parameter selection strategy for PWLS-ST- ℓ_1 , analyzes the proposed model by the empirical MSE and MMSE of its image update estimator, and performs more comprehensive comparisons with recent methods using both simulated and real clinical data.

The remainder of this paper is organized as follows. Section II describes the formulation for pre-learning STs, and proposes the MBIR model and algorithm for PWLS-ST- ℓ_1 . For the proposed algorithm, Section II introduces our preconditioner designs for sparse-view 2D fan-beam CT and 3D axial cone-beam CT, and proposes a new ADMM parameter selection scheme based on approximated condition numbers. Section II provides interpretations of the proposed model via analyzing the empirical MSE of its image update estimator, and the MMSE of its ℓ_2 -norm relaxed image update estimator. Section III reports detailed experimental results and comparisons to several recent methods. Section IV presents our conclusions and mentions future directions.

II. PROPOSED MODELS AND ALGORITHM

The proposed approach has two stages: training and testing. First, we learn a square ST from a dataset of high-quality CT images. Then, we apply the learned ST with ℓ_1 prior to reconstruct images from lower dose (or sparse-view) CT data. This section describes the formulation for pre-learning a square ST, proposes the PWLS reconstruction model using ℓ_1 prior with learned ST and its corresponding algorithm, and interprets the proposed model.

A. Offline Learning Sparsifying Transform

We pre-learn a ST by solving the following problem [30] (mathematical notations are detailed in Appendix A):

$$\underset{\Psi \in \mathbb{R}^{n \times n}}{\operatorname{argmin}} \min_{\{\mathbf{z}_j \in \mathbb{R}^n\}} \sum_{j=1}^{J'} \|\Psi \mathbf{x}_j - \mathbf{z}_j\|_2^2 + \gamma' \|\mathbf{z}_j\|_0 + \tau (\xi \|\Psi\|_F^2 - \log |\det \Psi|) \quad (1)$$

where $\Psi \in \mathbb{R}^{n \times n}$ is a square ST, $\{\mathbf{x}_j \in \mathbb{R}^n : j = 1, \dots, J'\}$ is a set of J' patches extracted from training data, $\mathbf{z}_j \in \mathbb{R}^n$ is the sparse code corresponding to the j th patch \mathbf{x}_j , n is the number of pixels (voxels) in each (vectorized) patch, J' is the total number of the image patches, and $\gamma', \tau, \xi > 0$ are regularization parameters.

B. CT Reconstruction Model Using ℓ_1 Prior with Learned Sparsifying Transform: PWLS-ST- ℓ_1

To reconstruct a linear attenuation coefficient image $\mathbf{x} \in \mathbb{R}^N$ from post-log measurement $\mathbf{y} \in \mathbb{R}^m$, we solve the following non-convex MBIR problem using PWLS and the ST Ψ learned via (1) [41]:

$$\underset{\mathbf{x} \in \mathbb{R}^N}{\operatorname{argmin}} \min_{\mathbf{z} \in \mathbb{R}^{nJ}} \frac{1}{2} \|\mathbf{y} - \mathbf{A}\mathbf{x}\|_{\mathbf{W}}^2 + \lambda \|\tilde{\Psi}\mathbf{x} - \mathbf{z}\|_1 + \gamma \|\mathbf{z}\|_0, \quad (\text{P})$$

where

$$\tilde{\Psi} = \begin{bmatrix} \Psi \mathbf{P}_1 \\ \vdots \\ \Psi \mathbf{P}_J \end{bmatrix} \quad \text{and} \quad \mathbf{z} = \begin{bmatrix} \mathbf{z}_1 \\ \vdots \\ \mathbf{z}_J \end{bmatrix}.$$

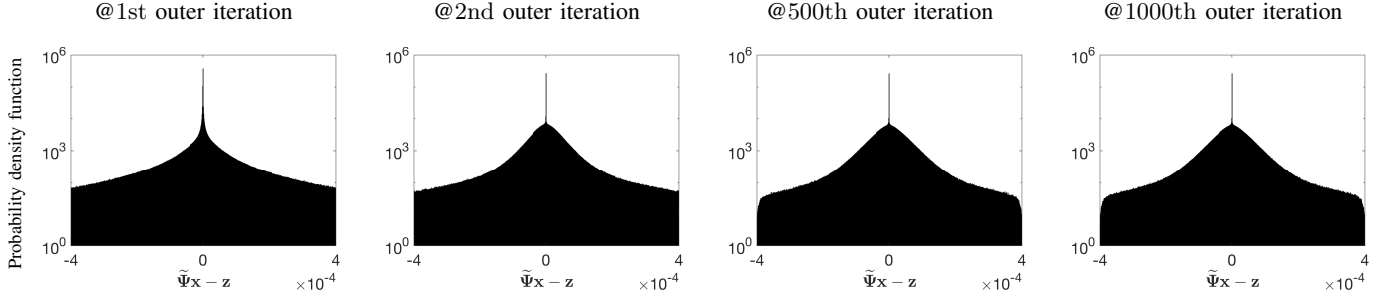


Fig. 1. Histograms of sparsification error $\tilde{\Psi}\mathbf{x} - \mathbf{z}$ at different outer iterations of the PWLS-ST- ℓ_2 method (in the XCAT phantom experiment with 2D fan-beam geometry and 12.5% (123) projection views). Y-axis uses a logarithmic scale, and the range of $\tilde{\Psi}\mathbf{x} - \mathbf{z}$ is within $[-4, 4] \times 10^{-4}$. Over the iterations, the sparsification error histograms appear more like a Laplace distribution than a Gaussian distribution.

Here, $\mathbf{A} \in \mathbb{R}^{m \times N}$ is a CT scan system matrix, $\mathbf{W} \in \mathbb{R}^{m \times m}$ is a diagonal weighting matrix with elements $\{W_{l,l} = \rho_l^2 / (\rho_l + \sigma^2) : l = 1, \dots, m\}$ based on a Poisson-Gaussian model for the pre-log measurements $\boldsymbol{\rho} \in \mathbb{R}^m$ with electronic readout noise variance σ^2 [42], $\mathbf{P}_j \in \mathbb{R}^{n \times N}$ is a patch-extraction operator for the j th patch, $\mathbf{z}_j \in \mathbb{R}^n$ is unknown sparse code for the j th patch, J is the number of extracted patches, and $\lambda, \gamma > 0$ are regularization parameters.

The term $\|\tilde{\Psi}\mathbf{x} - \mathbf{z}\|_1$ denotes a ℓ_1 -based sparsification error [3]–[5]. We expect ℓ_1 to be more robust to sparsity model mismatch than the ℓ_2 -based sparsification error $\|\tilde{\Psi}\mathbf{x} - \mathbf{z}\|_2^2$ used in [34], [36]. Fig. 1 shows histograms of sparsification error $\tilde{\Psi}\mathbf{x} - \mathbf{z}$ at different outer iterations of the PWLS-ST- ℓ_2 method. Over the iterations, the sparsification error histograms appear more like a Laplace distribution than a Gaussian distribution. This observation suggests that the proposed ℓ_1 prior model is more suitable than the ℓ_2 prior model for PWLS-ST-based reconstruction. Section III-B1 shows that the proposed ℓ_1 -based sparsification error term, $\|\tilde{\Psi}\mathbf{x} - \mathbf{z}\|_1$, improves the accuracy of reconstruction compared to the ℓ_2 prior model in [34], [36].

C. Proposed Algorithm for PWLS-ST- ℓ_1

To solve (P), our proposed algorithm alternates between updating the image \mathbf{x} (*image update step*) and the sparse codes \mathbf{z} (*sparse coding step*). For the image update, we apply ADMM [2], [9], [39] by introducing an auxiliary variable to separate the effects of a certain variable [9], [43]. For efficient sparse coding, we apply an analytical solution for \mathbf{z} . The following subsections provide details for solving (P), summarized in Algorithm 1, introduce our preconditioner designs, and describe a new ADMM parameter selection scheme based on approximated condition numbers.

1) *Image Update - ADMM*: Using the current sparse code estimates \mathbf{z} , we update the image \mathbf{x} by augmenting (P) with auxiliary variables [41]:

$$\begin{aligned} & \underset{\substack{\mathbf{x} \in \mathbb{R}^N, \mathbf{d}_a \in \mathbb{R}^m, \\ \mathbf{d}_\psi \in \mathbb{R}^{nJ}}}{\operatorname{argmin}} \quad \frac{1}{2} \|\mathbf{y} - \mathbf{d}_a\|_{\mathbf{W}}^2 + \lambda \|\mathbf{d}_\psi\|_1 \\ & \text{subject to} \quad \begin{bmatrix} \mathbf{d}_a \\ \mathbf{d}_\psi \end{bmatrix} = \begin{bmatrix} \mathbf{A} \\ \tilde{\Psi} \end{bmatrix} \mathbf{x} - \begin{bmatrix} \mathbf{0} \\ \mathbf{z} \end{bmatrix}. \end{aligned}$$

The corresponding augmented Lagrangian has the form

$$\begin{aligned} & \frac{1}{2} \|\mathbf{y} - \mathbf{d}_a\|_{\mathbf{W}}^2 + \lambda \|\mathbf{d}_\psi\|_1 + \frac{\mu}{2} \|\mathbf{d}_a - \mathbf{A}\mathbf{x} - \mathbf{b}_a\|_2^2 \\ & + \frac{\mu\nu}{2} \left\| \mathbf{d}_\psi - \left(\tilde{\Psi}\mathbf{x} - \mathbf{z} \right) - \mathbf{b}_\psi \right\|_2^2. \end{aligned}$$

We descend/ascend this augmented Lagrangian using the following iterative updates of the primal, auxiliary, dual variables $-\mathbf{x}$, $\{\mathbf{d}_a, \mathbf{d}_\psi\}$, and $\{\mathbf{b}_a, \mathbf{b}_\psi\}$, respectively:

$$\mathbf{G}\mathbf{x}^{(i+1)} = \mathbf{A}^T \left(\mathbf{d}_a^{(i)} - \mathbf{b}_a^{(i)} \right) + \nu \tilde{\Psi}^T \left(\mathbf{d}_\psi^{(i)} - \mathbf{b}_\psi^{(i)} + \mathbf{z} \right); \quad (2)$$

$$\mathbf{d}_a^{(i+1)} = \left(\mathbf{W} + \mu \mathbf{I}_m \right)^{-1} \left(\mathbf{W}\mathbf{y} + \mu \left(\mathbf{A}\mathbf{x}^{(i+1)} + \mathbf{b}_a^{(i)} \right) \right); \quad (3)$$

$$\mathbf{d}_{\psi,j}^{(i+1)} = \mathcal{S} \left(\left(\tilde{\Psi}\mathbf{x}^{(i+1)} - \mathbf{z} + \mathbf{b}_\psi^{(i)} \right)_j, \frac{\lambda}{\mu\nu} \right), j = 1, \dots, nJ;$$

$$\mathbf{b}_a^{(i+1)} = \mathbf{b}_a^{(i)} - \left(\mathbf{d}_a^{(i+1)} - \mathbf{A}\mathbf{x}^{(i+1)} \right);$$

$$\mathbf{b}_\psi^{(i+1)} = \mathbf{b}_\psi^{(i)} - \left(\mathbf{d}_\psi^{(i+1)} - \left(\tilde{\Psi}\mathbf{x}^{(i+1)} - \mathbf{z} \right) \right),$$

where the Hessian matrix $\mathbf{G} \in \mathbb{R}^{N \times N}$ is defined by

$$\mathbf{G} := \mathbf{A}^T \mathbf{A} + \nu \tilde{\Psi}^T \tilde{\Psi}, \quad (4)$$

Algorithm 1 PWLS-ST- ℓ_1 CT Reconstruction

Require: \mathbf{y} , $\mathbf{x}^{(1)}$, $\mathbf{z}^{(1)}$, $\tilde{\Psi}$ learned from (1), \mathbf{M} , \mathbf{W} , $\lambda, \gamma, \mu, \nu \geq 0$, $i = 1$

while a stopping criterion is not satisfied **do**

 Set $\mathbf{b}_a = \mathbf{b}_\psi = \mathbf{0}$

for $i' = 1, \dots, \text{Iter}_{\text{ADMM}}$ **do**

 Obtain $\mathbf{x}^{(i'+1)}$ by solving (2) with PCG(M)

$$\mathbf{d}_a^{(i'+1)} = \left(\mathbf{W} + \mu \mathbf{I}_m \right)^{-1} \left(\mathbf{W}\mathbf{y} + \mu \left(\mathbf{A}\mathbf{x}^{(i'+1)} + \mathbf{b}_a^{(i')} \right) \right)$$

$$\mathbf{d}_{\psi,j}^{(i'+1)} = \mathcal{S} \left(\left(\tilde{\Psi}\mathbf{x}^{(i'+1)} - \mathbf{z} + \mathbf{b}_\psi^{(i')} \right)_j, \frac{\lambda}{\mu\nu} \right), \forall j$$

$$\mathbf{b}_a^{(i'+1)} = \mathbf{b}_a^{(i')} - \left(\mathbf{d}_a^{(i'+1)} - \mathbf{A}\mathbf{x}^{(i'+1)} \right)$$

$$\mathbf{b}_\psi^{(i'+1)} = \mathbf{b}_\psi^{(i')} - \left(\mathbf{d}_\psi^{(i'+1)} - \left(\tilde{\Psi}\mathbf{x}^{(i'+1)} - \mathbf{z} \right) \right)$$

end for

$$\mathbf{z}_j^{(i+1)} = \mathcal{H} \left(\left(\tilde{\Psi}\mathbf{x}^{(\text{Iter}_{\text{ADMM}}+1)} \right)_j, \frac{\gamma}{\lambda} \right), \forall j$$

$i = i + 1$

end while

and the soft-shrinkage operator is defined by $\mathcal{S}(\alpha, \beta) := \text{sign}(\alpha) \max(|\alpha| - \beta, 0)$. Similar to [9, Fig. 1], we reset \mathbf{b}_a and \mathbf{b}_ψ as a zero-vector before running the ADMM image updates. To approximately solve (2), we use the preconditioned conjugate gradient (PCG) method with a preconditioner \mathbf{M} for the matrix \mathbf{G} in (4). PCG(\mathbf{M}) in Algorithm 1 denotes PCG method using a preconditioner \mathbf{M} . Section II-C3 describes details of the preconditioner designs.

2) *Sparse Coding*: Given the current estimates of the image \mathbf{x} , we update the sparse codes \mathbf{z} by solving the following optimization problem:

$$\min_{\mathbf{z} \in \mathbb{R}^{nJ}} \lambda \left\| \tilde{\Psi} \mathbf{x} - \mathbf{z} \right\|_1 + \gamma \|\mathbf{z}\|_0. \quad (5)$$

The optimal solution of (5) is given by an element-wise operator:

$$z_j^* = \mathcal{H} \left(\left(\tilde{\Psi} \mathbf{x} \right)_j, \frac{\gamma}{\lambda} \right), \quad j = 1, \dots, nJ, \quad (6)$$

where the hard-shrinkage operator $\mathcal{H}(\alpha, \beta)$ is defined equal to α for $|\alpha| \geq \beta$, and 0 otherwise.

3) *Preconditioner Designs for Solving (2) via PCG*: For a 2D fan-beam CT problem, a circulant preconditioner for the Hessian matrix \mathbf{G} defined in (4) is well suited because 1) it is effective for the “nearly” shift-invariant matrix $\mathbf{A}^T \mathbf{A}$ [2], [9] and 2) $\tilde{\Psi}^T \tilde{\Psi} = \sum_{j=1}^J \mathbf{P}_j^T \Psi^T \Psi \mathbf{P}_j$ is a block circulant circulant block (BCCB) matrix when we use the overlapping “stride” 1 and the “wrap around” image patch assumption. For an orthogonal transform Ψ , $\tilde{\Psi}^T \tilde{\Psi}$ is approximately $(n/\iota) \mathbf{I}_N$, where ι denotes the stride parameter. Therefore, a circulant preconditioner is a reasonable choice to approximate \mathbf{G} in (4) in 2D fan-beam CT.

For a 3D cone-beam CT problem, circulant preconditioning is less accurate because the matrix $\mathbf{A}^T \mathbf{A}$ is inherently shift-variant due to the system geometry and/or spatial variations in detector response [44]. Despite this fact, we select a circulant preconditioner to approximate \mathbf{G} in (4), and solve (2) in 3D CT reconstruction using more PCG inner iterations. The reason is three fold. First, a circulant preconditioner is still one of the classical options to approximate a shift-variant matrix (e.g., $\mathbf{A}^T \mathbf{A}$) and accelerate CG (see, for example, [44], [45]). Second, effective learned transforms are generally close to orthogonal (the same applies to the 2D case), and a scaled identity preconditioner can approximate the term $\tilde{\Psi}^T \tilde{\Psi}$. Third, a few PCG iterations in Algorithm 1 can provide fast convergence: 1) Fig. 2 shows that 2 and 5 PCG iterations give very similar convergence rates; 2) in the 3D CT reconstruction, the convergence rates of Algorithm 1 are comparable to those provided in 2D CT reconstruction – see Fig. 5. More sophisticated preconditioners might provide faster convergence [46], [47].

Considering the reasons above, we construct a circulant preconditioner \mathbf{M} [44] for the Hessian matrix \mathbf{G} defined in (4) as follows. We first approximate \mathbf{G} by

$$\mathbf{G} \approx \mathbf{Q}^H (\Lambda_A + \nu \Lambda_{\tilde{\Psi}}) \mathbf{Q}, \quad (7)$$

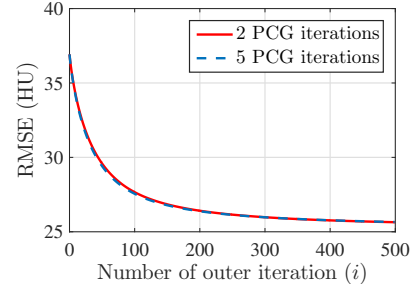


Fig. 2. Comparison of the RMSE convergence behavior for PWLS-ST- ℓ_1 with 2 and 5 PCG iterations in 3D cone-beam CT reconstruction (12.5% (123) views; $\lambda = 8 \times 10^6$, $\gamma/\lambda = 15$, $\kappa_{\text{des},\nu} = 10$, $\kappa_{\text{des},\mu} = 40$; RMSE stands for the root mean square error). Although a circulant preconditioner is known to be less accurate to approximate $\mathbf{A}^T \mathbf{A}$ in (4) for the 3D CT problem, Algorithm 1 using it with 2 PCG iterations gives a similar convergence rate compared to that with 5 PCG iterations.

where \mathbf{Q} is the orthogonal (2D or 3D) DFT matrix, and Λ_A and $\Lambda_{\tilde{\Psi}}$ are approximated eigenvalue matrices of $\mathbf{A}^T \mathbf{A}$ and $\tilde{\Psi}^T \tilde{\Psi}$ in \mathbf{G} . Next, we obtain Λ_A and $\Lambda_{\tilde{\Psi}}$ as follows:

$$\Lambda_A = \text{diag}(\text{fft}(\mathbf{A}^T \mathbf{A} \mathbf{e}_c)) \quad \text{and} \quad \Lambda_{\tilde{\Psi}} = \text{diag}(\text{fft}(\tilde{\Psi}^T \tilde{\Psi} \mathbf{e}_c)), \quad (8)$$

where $\text{diag}(\cdot)$ denotes the conversion of a vector into a diagonal matrix, $\text{fft}(\cdot)$ denotes the (2D or 3D) fast Fourier transforms (FFT), and \mathbf{e}_c is a standard basis vector corresponds to the center pixel of the image. Finally, we construct $\mathbf{M} = \mathbf{Q}^H (\Lambda_A + \nu \Lambda_{\tilde{\Psi}})^{-1} \mathbf{Q}$. For PCG(\mathbf{M}) in Algorithm 1, we use (inverse) FFTs to compute the circulant preconditioner \mathbf{M} designed above.

4) *Parameter Selection based on Condition Numbers*:

In practice, ADMM can require difficult parameter tuning processes for fast and stable convergence. We moderate this problem by selecting ADMM parameters (e.g., ν, μ) based on (approximated) condition numbers [9]. Observe that, for two square Hermitian matrices $\mathbf{A} \succeq 0$ and $\mathbf{B} \succ 0$,

$$\kappa(\mathbf{A} + \mathbf{B}) := \frac{\sigma_{\max}(\mathbf{A} + \mathbf{B})}{\sigma_{\min}(\mathbf{A} + \mathbf{B})} \leq \frac{\sigma_{\max}(\mathbf{A}) + \sigma_{\max}(\mathbf{B})}{\sigma_{\min}(\mathbf{A}) + \sigma_{\min}(\mathbf{B})}, \quad (9)$$

by Weyl’s inequality, where the notations $\kappa(\cdot)$, $\sigma_{\max}(\cdot)$, and $\sigma_{\min}(\cdot)$ denote the condition number, the largest eigenvalue, and the smallest eigenvalue of a matrix, respectively.

Applying the bound (9) to the Hessian matrix \mathbf{G} defined in (4), we select ν by

$$\nu = \frac{\sigma_{\max}(\Lambda_A) - \kappa_{\text{des},\nu} \cdot \sigma_{\min}(\Lambda_A)}{\kappa_{\text{des},\nu} \cdot \sigma_{\min}(\Lambda_{\tilde{\Psi}}) - \sigma_{\max}(\Lambda_{\tilde{\Psi}})}, \quad (10)$$

where $\kappa_{\text{des},\nu}$ denotes the desired “upper bounded” condition number of the matrix \mathbf{G} , and Λ_A and $\Lambda_{\tilde{\Psi}}$ are given as in (8). (The eigenvalue approximation for $\mathbf{A}^T \mathbf{A}$ and $\tilde{\Psi}^T \tilde{\Psi}$ can be improved by the power iteration used in [9], with a cost of higher computational complexity.) Note that equality holds in (9) when either \mathbf{A} or \mathbf{B} is a scaled identity matrix. In other words, when the learned ST Ψ is close to orthogonal, i.e., $\tilde{\Psi}^T \tilde{\Psi} \approx (n/\iota) \mathbf{I}_N$, $\kappa_{\text{des},\nu}$ becomes close to the condition number of the approximated \mathbf{G} in (7). Applying the bound (9) to the Hessian matrix $\mathbf{W} + \mu \mathbf{I}_m$ of (3), we select μ by

$$\mu = \frac{\sigma_{\max}(\mathbf{W}) - \kappa_{\text{des},\mu} \cdot \sigma_{\min}(\mathbf{W})}{\kappa_{\text{des},\mu} - 1}, \quad (11)$$

where $\kappa_{\text{des},\mu}$ denotes the desired condition number of $\mathbf{W} + \mu\mathbf{I}_m$.

The proposed ADMM parameter selection scheme using (approximated) condition numbers has several benefits over direct ADMM parameter tuning:

- Suppose that a CT geometry, i.e., the system matrix \mathbf{A} and a square ST Ψ are fixed. For different measurements, one would not need to tune the ADMM parameter ν in (2), because the system matrix \mathbf{A} in (2) is fixed; however, the ADMM parameter μ in (3) requires tuning processes, because the weighting matrix \mathbf{W} in (3) depends on the pre-log measurements $\boldsymbol{\rho}$. The proposed ADMM parameter selection scheme above can moderate the issue of tuning the ADMM parameter μ by using a desired condition number $\kappa_{\text{des},\mu}$.
- We found that 1) the well-tuned desired condition numbers $\kappa_{\text{des},\nu}, \kappa_{\text{des},\mu}$ in one representative CT image reconstruction case, work well in different CT datasets, including real clinical data (see details in Section III-B4); 2) $\kappa_{\text{des},\nu}$ is robust to mild variations in CT system matrix \mathbf{A} , for example, 2D fan-beam CT and 3D axial CT scans (see details in Sections III-A3 & III-A5).
- It is more intuitive to tune the desired condition numbers, $\kappa_{\text{des},\nu}$ and $\kappa_{\text{des},\mu}$, compared to directly tuning their corresponding ADMM parameters, ν and μ . We empirically found that $\kappa_{\text{des},\nu}, \kappa_{\text{des},\mu} \in [10, 50]$ are reasonable values for fast and stable convergence of Algorithm 1.

D. Interpreting the Proposed Model (P)

This section interprets the proposed PWLS-ST- ℓ_1 reconstruction model (P). Signal $\mathbf{x}^{(i)}$ should be sparse in the learned transform ($\tilde{\Psi}$)-domain. Particularly, $\tilde{\Psi}\mathbf{x}^{(i)}$ should have a few large and some small coefficients that usually correspond to local high-frequency features (e.g., edges) and noisy features, respectively. Thresholding in the sparse coding step removes the small signal coefficients (hopefully noise) while preserving the large ones. Using the “denoised” sparse codes $\mathbf{z}^{(i)}$ for the next image update, the method balances the data fidelity (i.e., $\frac{1}{2}\|\mathbf{y} - \mathbf{A}\mathbf{x}\|_{\mathbf{W}}^2$) and the learned ℓ_1 prior (i.e., $\lambda\|\tilde{\Psi}\mathbf{x} - \mathbf{z}^{(i)}\|_1$) that is robust to the model mismatch between $\tilde{\Psi}\mathbf{x}$ and $\mathbf{z}^{(i)}$, $\forall i$. Repeating these processes refines the reconstructed image.

Given $\mathbf{z}^{(i)}$, the update of \mathbf{x} in (P) would be

$$\mathbf{x}^{(i+1)} = \underset{\mathbf{x} \in \mathbb{R}^N}{\text{argmin}} \frac{1}{2}\|\mathbf{y} - \mathbf{A}\mathbf{x}\|_{\mathbf{W}}^2 + \lambda\|\tilde{\Psi}\mathbf{x} - \mathbf{z}^{(i)}\|_1. \quad (12)$$

One can expect the update $\mathbf{x}^{(i+1)}$ to improve, as the denoised sparse codes $\mathbf{z}^{(i)}$ become closer to those of the true signal \mathbf{x}^{true} . To support this argument, we empirically calculated MSE of the following estimator: $\hat{\mathbf{x}} = \underset{\mathbf{x} \in \mathbb{R}^N}{\text{argmin}} \frac{1}{2}\|\mathbf{y} - \mathbf{A}\mathbf{x}\|_{\mathbf{W}}^2 + \lambda\|\tilde{\Psi}\mathbf{x} - \mathbf{z}\|_1$. In particular, we solved the above optimization problem by the image updating iterations in Algorithm 1 with a hundred random realizations of \mathbf{z} , where we randomly generated \mathbf{z} by corrupting $\tilde{\Psi}\mathbf{x}^{\text{true}}$ with three different levels – 10, 20, and 30dB signal-to-noise ratio (SNR) – of random additive white Gaussian noise. For \mathbf{z} with 10, 20, and, 30 dB SNR levels, the empirical MSE values of the estimator $\hat{\mathbf{x}}$ were (approximately) 9.4×10^7 , 1.2×10^7 ,

and 1.3×10^6 , respectively – in Hounsfield units, HU¹. These empirical results support that the better the quality of $\mathbf{z}^{(i)}$, the more accurate $\mathbf{x}^{(i+1)}$ in (12).

We formally state the above intuition by relaxing the ℓ_1 -norm with a ℓ_2 -norm in (12) in the following.

Proposition 1. Consider the following model:

$$\mathbf{y} = \mathbf{A}\mathbf{x}^{\text{true}} + \boldsymbol{\varepsilon} \quad \text{and} \quad \mathbf{z}^{(i)} = \tilde{\Psi}\mathbf{x}^{\text{true}} + \mathbf{e}^{(i)}, \quad (13)$$

where $\mathbf{y} \in \mathbb{C}^m$ is a measurement vector, $\mathbf{A} \in \mathbb{C}^{m \times N}$ is a system matrix, $\tilde{\Psi} \in \mathbb{C}^{N' \times N}$ is a sparsifying transform with $N' \geq N$, $\mathbf{z}^{(i)} \in \mathbb{C}^{N'}$ is the denoised signal at the $(i-1)$ th iteration, and the noise vector $\boldsymbol{\varepsilon} \in \mathbb{C}^m$ and error vector $\mathbf{e}^{(i)} \in \mathbb{C}^{N'}$ are assumed to follow zero-mean Gaussian distribution, i.e., $\boldsymbol{\varepsilon} \sim \mathcal{N}(\mathbf{0}, \mathbf{C}_{\boldsymbol{\varepsilon}})$ and $\mathbf{e}^{(i)} \sim \mathcal{N}(\mathbf{0}, \mathbf{C}_{e,i})$, where $\mathbf{C}_{\boldsymbol{\varepsilon}} \in \mathbb{C}^{m \times m}$ and $\mathbf{C}_{e,i} \in \mathbb{C}^{N' \times N'}$ are covariance matrices. Assuming that $\boldsymbol{\varepsilon}$ and $\mathbf{e}^{(i)}$ are uncorrelated, the minimum-variance unbiased estimator (MVUE) is given by

$$\mathbf{x}^{(i+1)} = \left(\mathbf{A}^H \mathbf{C}_{\boldsymbol{\varepsilon}}^{-1} \mathbf{A} + \tilde{\Psi}^H \mathbf{C}_{e,i}^{-1} \tilde{\Psi} \right)^{-1} \cdot \left(\mathbf{A}^H \mathbf{C}_{\boldsymbol{\varepsilon}}^{-1} \mathbf{y} + \tilde{\Psi}^H \mathbf{C}_{e,i}^{-1} \mathbf{z}^{(i)} \right). \quad (14)$$

Assuming that $\mathbf{A}^H \mathbf{A}$ and $\tilde{\Psi}^H \tilde{\Psi}$ are decomposed by some identical orthogonal matrices, and setting $\mathbf{C}_{\boldsymbol{\varepsilon}} = \sigma_{\boldsymbol{\varepsilon}}^2 \mathbf{I}$ and $\mathbf{C}_{e,i} = \sigma_{e,i}^2 \mathbf{I}$, the minimum variance (i.e., the MMSE for unbiased estimator)² of the solution (14) is given by

$$\text{var}(\mathbf{x}^{(i+1)}) = \sum_{j=1}^N \frac{1}{\frac{1}{\sigma_{\boldsymbol{\varepsilon}}^2} (\lambda_A)_j + \frac{1}{\sigma_{e,i}^2} (\lambda_{\tilde{\Psi}})_j}, \quad (15)$$

where $\{(\lambda_A)_j \geq 0 : \forall j\}$ and $\{(\lambda_{\tilde{\Psi}})_j \geq 0 : \forall j\}$ are the spectrum of $\mathbf{A}^H \mathbf{A}$ and $\tilde{\Psi}^H \tilde{\Psi}$, respectively.

Proposition 1 is the first analytical result that quantifies the performance of learned analysis regularizers (e.g., learned convolutional analysis operator [24] and learned transform [30]) in signal recovery. When the ℓ_1 -norm is relaxed with a ℓ_2 -norm (and setting $\mathbf{W} = \mathbf{C}_{\boldsymbol{\varepsilon}}^{-1}$ and $\lambda = 1/\sigma_{e,i}^2$), the MVUE solution in (14) with $\mathbf{C}_{e,i} = \sigma_{e,i}^2 \mathbf{I}$ corresponds to that of the image update problem (12). The assumption of uncorrelated $\boldsymbol{\varepsilon}$ and $\mathbf{e}^{(i)}$ is satisfied, if the noise in the measurement domain and the error in the $\tilde{\Psi}$ -domain are uncorrelated.

For any \mathbf{A} and $\tilde{\Psi}$, the minimum variance $\text{var}(\mathbf{x}^{(i+1)})$ in (15) can be further reduced as the error variance $\sigma_{e,i}^2$ becomes smaller, for some fixed $\sigma_{\boldsymbol{\varepsilon}}^2 \in (0, \infty)$. For example, if $\sigma_{e,i}^2 \rightarrow \epsilon$, where $0 < \epsilon \ll 1$, then $\text{var}(\mathbf{x}^{(i+1)})$ becomes very small. If the “denoised” sparse codes $\mathbf{z}^{(i)}$ become close to $\tilde{\Psi}\mathbf{x}^{\text{true}}$ as $i \rightarrow \infty$, one obtains accurate image reconstruction after sufficiently iterating the updates for (P) in Algorithm 1. To better “denoise” the update $\mathbf{x}^{(i+1)}$ in particular, we pre-learn a ST Ψ via (1) from high-quality training datasets.

¹Modified Hounsfield units, where air is 0 HU and water is 1000 HU.

²Rigorously speaking, so called variance or MSE in our paper is the sum of pixel-wise variances or MSEs (i.e., trace of variance matrix or MSE matrices, e.g., $\text{tr}(\text{Var}(\cdot))$). For brevity, we refer the $\text{tr}(\text{Var}(\cdot))$ as variance.

III. RESULTS AND DISCUSSIONS

A. Experimental Setup

We evaluated the proposed PWLS-ST- ℓ_1 method for sparse-view CT reconstruction with 2D fan-beam and 3D axial cone-beam scans of a XCAT phantom that has overall 500 slices [40]. We also evaluated PWLS-ST- ℓ_1 for sparse-view CT reconstruction with 2D fan-beam real GE clinical data. We compared the quality of images reconstructed by PWLS-ST- ℓ_1 with those of:

- *FBP*: Conventional filtered back-projection method using a Hanning window (for 3D experiments, the Feldkamp-Davis-Kress method [48] was used).
- *PWLS-EP*: Conventional MBIR method using PWLS and an edge-preserving regularizer $\sum_{j=1}^N \sum_{k \in N_j} \iota_j \iota_k \varphi(x_j - x_k)$, where N_j is the set of neighbors of x_j , ι_j and ι_k are regularization parameters that encourage uniform noise [49], and $\varphi(t) := \delta^2 \left(\sqrt{1 + |t/\delta|^2} - 1 \right)$ for 2D, $\varphi(t) := \delta^2 (|t/\delta| - \log(1 + |t/\delta|))$ for 3D ($\delta = 10$ HU). We adopted the relaxed linearized augmented Lagrangian method with ordered-subsets (relaxed OS-LALM) proposed in [50] to accelerate the reconstruction.
- *PWLS-ST- ℓ_2* (Zheng et al., 2018): MBIR method using PWLS and ℓ_2 prior with a learned ST [34], [36]. For fair comparison, we performed the image update of the algorithm proposed for PWLS-ST- ℓ_2 without the non-nonnegativity constraint.
- *PWLS-DL* (Xu et al., 2012): MBIR method using PWLS and ℓ_2 prior with a learned overcomplete synthesis dictionary [31]. We replaced the separable quadratic surrogate method with ordered-subsets based acceleration (SQS-OS) in [31] with relaxed OS-LALM to accelerate image updates. For fair comparison, we ran this method without the non-nonnegativity constraint. PWLS-DL is far slower for 3D reconstruction with large 3D patches, compared to 2D reconstruction [36]; thus, we focus our comparisons between PWLS-ST- ℓ_1 and PWLS-DL for 2D reconstruction.
- *FBPConvNet* (Jin et al., 2017): A non-MBIR “denoising” method whose network structure is modified from U-Net [14]. As suggested in [14], we trained the network by minimizing the ℓ_2 -based training loss function that used paired training images – specifically, pairs of ground truth images and their noisy versions reconstructed by applying FBP to (simulated) undersampled sinograms.

We quantitatively evaluated the reconstruction quality in phantom experiments by RMSE (in HU) in a region of interest (ROI). The RMSE is defined by $\text{RMSE} := \left(\sum_{j=1}^{N_{\text{ROI}}} (\hat{x}_j - x_j^{\text{true}})^2 / N_{\text{ROI}} \right)^{1/2}$, where \hat{x} is the reconstructed image (after clipping negative values), x^{true} is the ground truth image, and N_{ROI} is the number of pixels in a ROI.

1) *2D Fan-Beam - Imaging*: To avoid an inverse crime, our 2D imaging simulation used a 840×840 slice (air cropped, $\Delta_x = \Delta_y = 0.4883$ mm) of the XCAT phantom, which was different from the training slices. We simulated sinograms of size 888 (detector channels) \times $\{246, 123\}$ (regularly spaced projection views or angles; 984 is the number of full views)

with GE LightSpeed fan-beam geometry corresponding to a monoenergetic source with $\rho_0 = 10^5$ incident photons per ray and no background events, and electronic noise variance $\sigma^2 = 5^2$. We reconstructed a 420×420 image with a coarser grid, where $\Delta_x = \Delta_y = 0.9766$ mm. The ROI here was a circular (around center) region containing all the phantom tissues.

The clinical chest data was collected by the GE scanner using the same CT geometry described above. We reconstructed a 716×716 image with $\Delta_x = \Delta_y = 0.9777$ mm. The tube voltage and tube current were 120 kVp and 160 mA, respectively.

2) *2D Fan-Beam - Training*: Before executing reconstructions with the PWLS-ST- ℓ_1 , PWLS-ST- ℓ_2 , PWLS-DL, and FBPConvNet methods, we pre-learned or trained their priors or networks from training data. For the PWLS-ST- ℓ_1 and PWLS-ST- ℓ_2 methods, we learned square (64×64) STs from 8×8 image patches extracted from five different slices of the XCAT phantom (with 1×1 overlapping stride). To learn well-conditioned transforms, we chose a large enough τ , e.g., $\tau = 5.85 \times 10^{14}$. We chose $\gamma' = 110$ and $\xi = 1$. Initialized with the 2D discrete cosine transform (DCT), we ran 1000 iterations of the alternating minimization algorithm proposed in [30] to ensure learned transforms were well converged. For PWLS-DL, we learned a 64×256 -sized overcomplete dictionary from the same set of 8×8 -sized patches used in learning square STs (see above). We used a maximum patch-wise sparsity level of 20 and a sparse coding error threshold of 10^{-1} . In FBPConvNet training, we used 390 paired images for training (each image corresponded to a slice of the XCAT phantom). Note that the testing phantom image is sufficiently different from training phantom images (specifically, they are at least 3.3cm away from training images). We used FBP-reconstructed images from the sparse-view sinograms simulated in Section III-A1 and the ground truth images of the XCAT phantom (with no noise), as training pairs. We trained networks using the data augmentation strategy and optimization method (i.e., stochastic gradient descent method) suggested in [14]. We set training hyperparameters (similar to those used in [14]) as follows: 151 epochs; learning rate decreased logarithmically from 10^{-2} to 10^{-3} ; batch size of 1; “momentum” parameter 0.99; and the clipping value for gradient of 10^{-2} .

3) *2D Fan-Beam - Image Reconstruction*: This section describes parameters used in reconstruction experiments with the XCAT phantom data and the clinical chest data. In XCAT phantom experiments, we initialized the PWLS-EP method with FBP reconstructions, and ran the relaxed OS-LALM [50] for 100 iterations with 12 ordered subsets. We chose the regularization parameter (balancing the data fitting term and the regularizer) as $2^{15.5}$ and $2^{15.0}$ for 246 and 123 views, respectively. For both PWLS-ST- ℓ_1 and PWLS-ST- ℓ_2 methods, we used a patch size 8×8 with a 1×1 overlapping stride. We used converged PWLS-EP reconstructions for initialization and set a stopping criterion as meeting the maximum number of iterations, e.g., $\text{Iter} = 1000$. For the image update, we set $\text{Iter}_{\text{ADMM}} = 2$ (2 PCG iterations [9]) for PWLS-ST- ℓ_1 ; and set 12 relaxed OS-LALM iterations without ordered subsets for PWLS-ST- ℓ_2 . For PWLS-ST- ℓ_1 , we tuned ν, μ using the

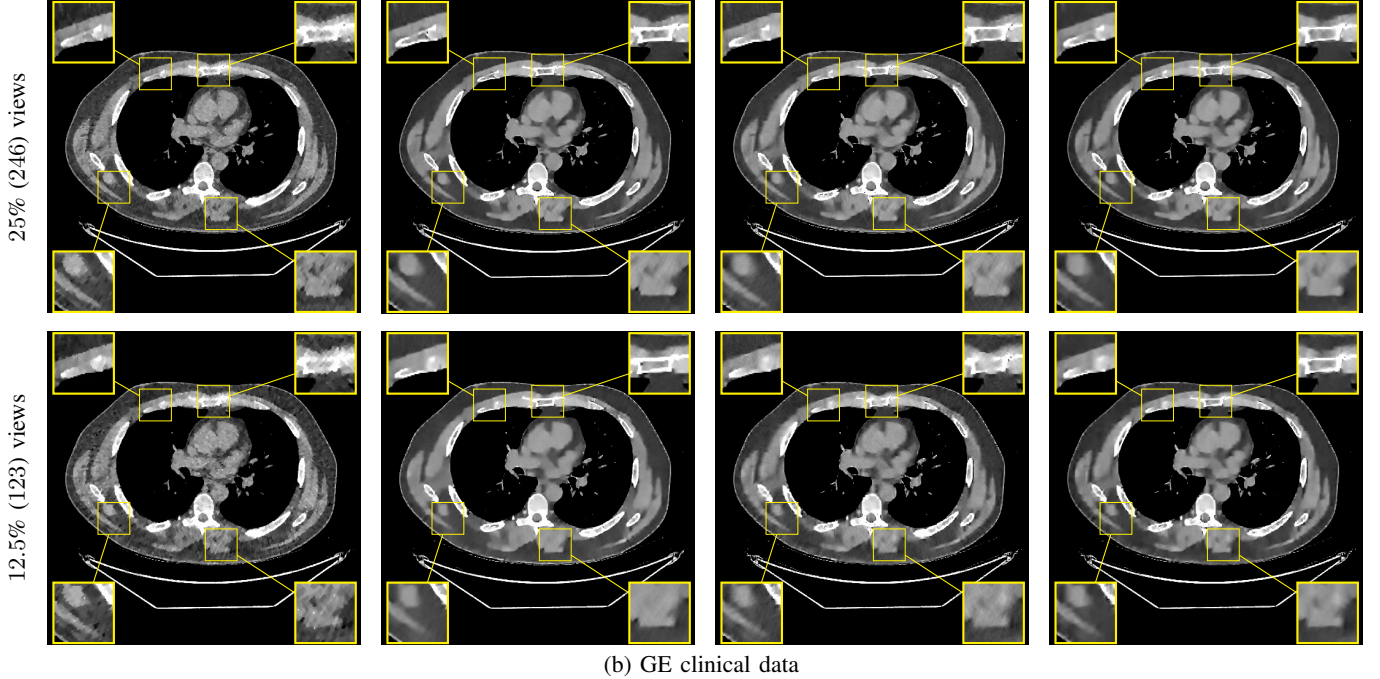
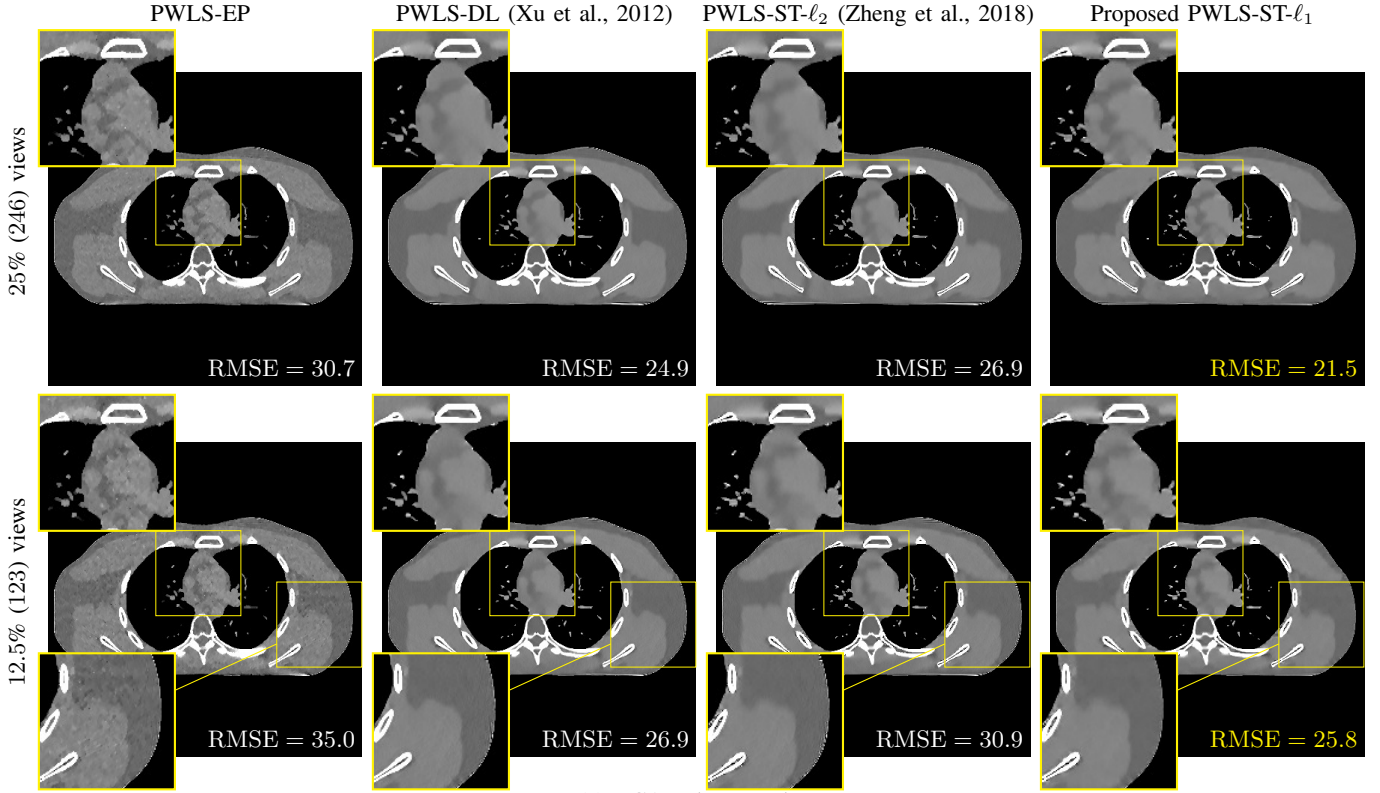


Fig. 3. Comparison of 2D reconstructed images from different MBIR methods with different number of views (2D fan-beam CT geometry; display window is [800, 1200] HU). See the reference images and reconstructed images via FBP in Fig. 6 and Fig. S.2, respectively. See the error maps between the reconstructed images and the ground truth for (a) in Fig. S.6 in the supplement.

condition number based selection schemes, i.e., $\kappa_{des,\nu}$ in (10) and $\kappa_{des,\mu}$ in (11). We finely tuned the parameters λ, γ to achieve good image quality. For PWLS-ST- ℓ_1 , we chose $\{\lambda, \gamma/\lambda, \kappa_{des,\nu}, \kappa_{des,\mu}\}$ as follows: $\{1.3 \times 10^6, 80, 30, 30\}$ for 246 views; $\{9 \times 10^5, 80, 30, 30\}$ for 123 views. For PWLS-ST- ℓ_2 , we chose $\{\lambda, \gamma\}$ as follows: $\{3 \times 10^5, 20\}$ for 246 views;

$\{1.6 \times 10^5, 20\}$ for 123 views. Note that λ and γ are in HU. For PWLS-DL, we chose a maximum sparsity level of 25, set an error tolerance as 60, and set a regularization parameter as 1.3×10^5 and 7×10^4 for 246 and 123 views, respectively. Similar to the PWLS-ST method, we finely tuned these parameters to achieve good image quality.

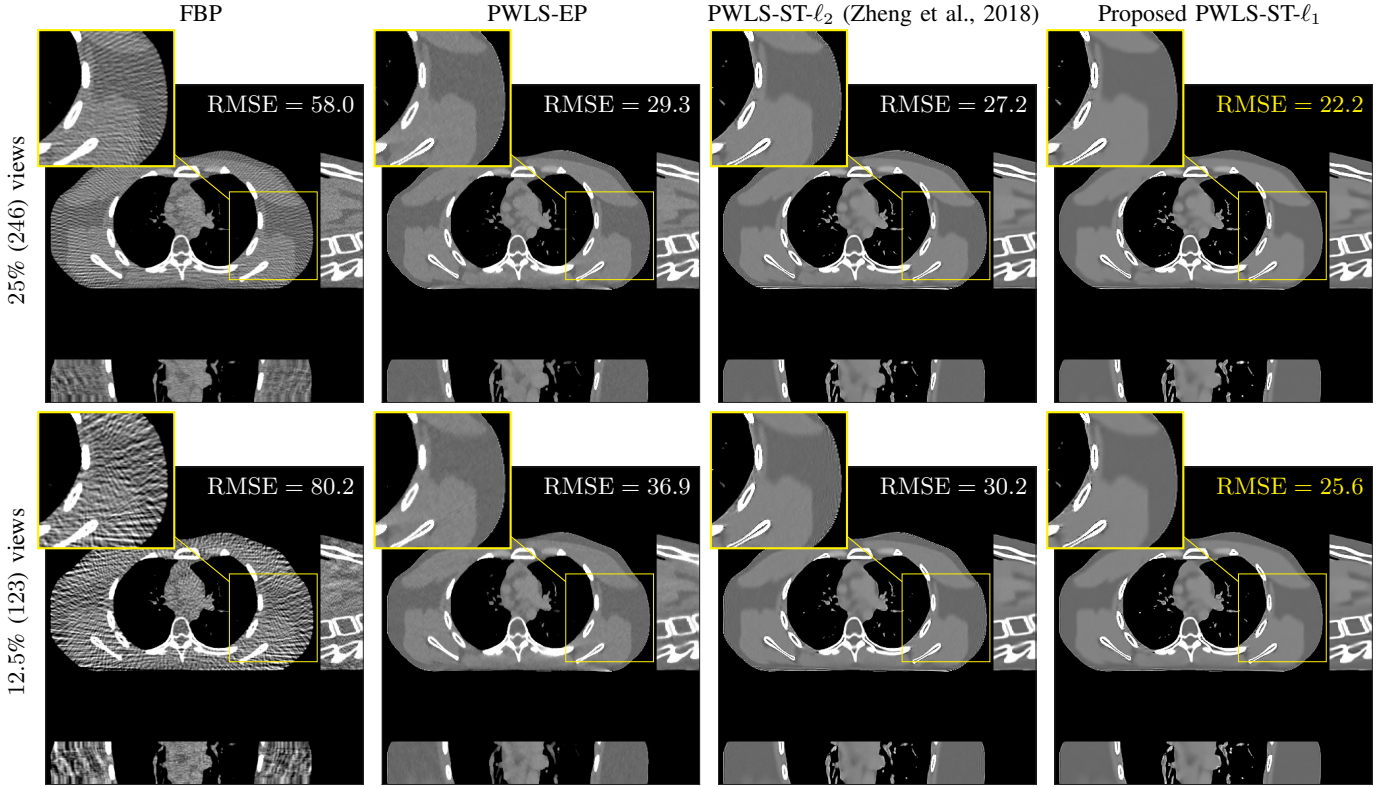


Fig. 4. Comparison of 3D reconstructed images from different X-ray CT reconstruction methods with different number of views (axial 3D cone-beam geometry; display window is [800, 1200] HU; displayed for the central axial, sagittal, and coronal planes; see the ground truth in Fig. S.4 in the supplement.)

In clinical data reconstruction, unless stated otherwise, we used the same learned models, trained networks, and reconstruction parameter sets listed above. We initialized all methods with FBP reconstructions. For PWLS-EP, we ran the relaxed OS-LALM for 50 iterations with 6 ordered subsets, and chose the regularization parameter as $2^{2.5}$ and 2^2 for 246 and 123 views, respectively. For PWLS-ST- ℓ_1 , we used the identical $\kappa_{des,\nu}$, $\kappa_{des,\mu}$, γ/λ values chosen in the XCAT phantom experiments. To automatically select the regularization parameter λ , we used the guideline described in Section III-B4, and it is chosen as approximately 1.2×10^{-2} and 8×10^{-3} for 246 and 123 views, respectively. For PWLS-ST- ℓ_2 , we chose $\{\lambda, \gamma\}$ as follows: $\{10^{-3}, 35\}$ for 246 views; $\{5 \times 10^{-4}, 40\}$ for 123 views. For PWLS-DL, we chose a maximum sparsity level of 25, set an error tolerance as 85, and set a regularization parameter as 7×10^{-4} and 6×10^{-4} for 246 and 123 views, respectively.

4) *3D Cone-Beam - Imaging*: In the 3D CT experiments, we simulated an axial cone-beam CT scan using an $840 \times 840 \times 96$ volume from the XCAT phantom (air cropped, $\Delta_x = \Delta_y = 0.4883$ mm and $\Delta_z = 0.625$ mm). We generated sinograms of size 888 (detector channels) $\times 64$ (detector rows) $\times \{246, 123\}$ (984 is the number of full views) using GE LightSpeed cone-beam geometry corresponding to a monoenergetic source with $\rho_0 = 10^5$ incident photons per ray and no scatter, and $\sigma^2 = 5^2$. We reconstructed a $420 \times 420 \times 96$ volume with a coarser grid, where $\Delta_x = \Delta_y = 0.9766$ mm and $\Delta_z = 0.625$ mm. We defined a cylinder ROI for the 3D case, which consisted of the central 64 of 96 axial slices and a circular (around center)

region in each slice. The diameter of the circle was 420 pixels, which is the width of each slice.

5) *3D Cone-Beam - Training and Image Reconstruction*: Similar to the 2D experiments, we pre-learned square STs using $8 \times 8 \times 8$ patches (with an overlapping stride $2 \times 2 \times 2$) extracted from a $420 \times 420 \times 54$ volume of the XCAT phantom, which is different from the volume used for testing. Initialized with the 3D DCT, we ran the transform learning algorithm [30] for 1000 iterations with $\tau = 5.63 \times 10^{15}$, $\gamma' = 100$ and $\xi = 1$.

For the PWLS-EP method, initialized with FBP reconstructions, we ran the relaxed OS-LALM for 100 iterations with 12 subsets and regularization parameter of 2^{14} , for both 246 and 123 views. For both PWLS-ST- ℓ_1 and PWLS-ST- ℓ_2 , we chose an $8 \times 8 \times 8$ patch size with a patch stride $3 \times 3 \times 3$. Initialized with converged PWLS-EP reconstructions, we chose a maximum number of iterations $\text{Iter} = 500$ as the stopping criterion. For the image update, we set $\text{Iter}_{\text{ADMM}}$ as 2 (we empirically found that 2 PCG iterations provide reasonable convergence behavior, see Fig. 2) for PWLS-ST- ℓ_1 , and set 2 relaxed OS-LALM iterations with 4 ordered subsets for PWLS-ST- ℓ_2 [36]. For PWLS-ST- ℓ_1 , we chose $\{\lambda, \gamma/\lambda, \kappa_{des,\nu}, \kappa_{des,\mu}\}$ as follows: $\{10^7, 15, 10, 50\}$ for 246 views; $\{8 \times 10^6, 15, 10, 40\}$ for 123 views. For PWLS-ST- ℓ_2 , we chose $\{\lambda, \gamma\}$ as follows: $\{10^6, 18\}$ for 246 views; $\{8 \times 10^5, 18\}$ for 123 views.

B. Results and Discussion

1) *Reconstruction Comparisons among Different MBIR Methods*: This section compares the reconstruction quality

and runtime among the proposed MBIR method, PWLS-ST- ℓ_1 , and other three MBIR methods, PWLS-EP, PWLS-DL, and PWLS-ST- ℓ_2 . Table I shows that, for both 2D and 3D sparse-view CT reconstructions of the XCAT phantom, the proposed PWLS-ST- ℓ_1 model outperforms PWLS-EP and PWLS-ST- ℓ_2 in terms of RMSE. In addition, PWLS-ST- ℓ_1 using a square transform (of size 64×64) achieves lower RMSE than PWLS-DL using an overcomplete dictionary (of size 64×256) for 2D sparse-view reconstructions. Fig. 3(a) and Fig. 4 show the reconstructed images for 2D and 3D phantom experiments, with different reconstruction models and different number of views. (See the corresponding error maps in the supplement.) The proposed PWLS-ST- ℓ_1 consistently gives more accurate image reconstructions compared to other MBIR methods. Specifically, PWLS-ST- ℓ_1 has smaller errors in the heart region (see zoom-ins in Fig. 3(a)) of 2D reconstructions than PWLS-DL and PWLS-ST- ℓ_2 . In addition, compared to PWLS-ST- ℓ_1 , PWLS-DL and PWLS-ST- ℓ_2 have some ringing artifacts around the edges with high transition, e.g., edges between air and soft tissues. (See a comparison of profiles of PWLS-ST- ℓ_1 and PWLS-ST- ℓ_2 in the supplement.) In particular, PWLS-ST- ℓ_2 and PWLS-DL give more visible ringing artifacts for 2D reconstruction from fewer views, and PWLS-ST- ℓ_2 has these ringing artifacts for 3D reconstructions regardless of the number of views (see zoom-ins in Fig. 4). Table II reports runtimes of different MBIR methods in reconstructing the 123-views XCAT phantom scan. (FBPConvNet is a non-MBIR method and its runtime for processing a 512×512 image is approximately one second with a TITAN Xp GPU.) While providing better reconstruction quality, the proposed Algorithm 1 of PWLS-ST- ℓ_1 has shorter runtime compared to the algorithms of PWLS-DL and PWLS-ST- ℓ_2 in Section III-A. Similar to the PWLS-EP algorithm, the reconstruction time of the PWLS-DL, PWLS-ST- ℓ_2 , and PWLS-ST- ℓ_1 algorithms can be further reduced by using ordered subsets [51].

Fig. 3(b) shows that when tested on the clinical scan data, the proposed PWLS-ST- ℓ_1 method improves reconstruction quality in terms of noise and artifacts removal (e.g., see zoom-ins for soft-issue regions), and edge preservation (e.g., see zoom-ins for bone regions), compared to PWLS-EP and PWLS-ST- ℓ_2 . Compared to PWLS-DL, PWLS-ST- ℓ_1 achieves comparable image quality, but requires less computational complexity.

The benefit of the proposed PWLS-ST- ℓ_1 over PWLS-ST- ℓ_2 can be explained when there exist some outliers for some $\mathbf{z}^{(i)}$: $\|\tilde{\Psi}\mathbf{x} - \mathbf{z}^{(i)}\|_1$ in (12) gives equal emphasis to all sparse codes – from small to large coefficients that generally correspond to edges in low- and high-contrast regions, respectively – in estimating \mathbf{x} ; however, PWLS-ST- ℓ_2 adjusts \mathbf{x} to mainly minimize the outliers, i.e., it may not pay enough attention to reconstruct regions with small coefficients. The histogram results in Fig. 1 reveal model mismatch of PWLS-ST- ℓ_2 over the iterations. Fig. 3, Fig. 4, and Table I show that PWLS-ST- ℓ_1 can moderate model mismatch, and provides more accurate reconstruction than PWLS-ST- ℓ_2 .

2) *Algorithm Convergence Rate*: Our main concern in convergence rates of Algorithm 1 lies with an inaccurate preconditioner (e.g., circulant one) particularly for the 3D

TABLE I
RMSE (HU) OF DIFFERENT 2D AND 3D X-RAY CT RECONSTRUCTIONS WITH DIFFERENT NUMBER OF PROJECTION VIEWS (XCAT PHANTOM EXPERIMENTS)

	Views ^a	FBP	PWLS-EP	PWLS-DL	PWLS-ST- ℓ_2	PWLS-ST- ℓ_1
2D ^b	246	60.5	30.7	24.9	26.9	21.5
	123	82.7	35.0	26.9	30.9	25.8
3D ^c	246	58.0	29.3	-	27.2	22.2
	123	80.2	36.9	-	30.2	25.6

^aThe 246 and 123 projection views correspond to 25% and 12.5% of the full views, 984, respectively.

^bFor the 2D CT experiments, fan-beam geometry was used.

^cFor the 3D CT experiments, axial cone-beam geometry was used.

TABLE II
COMPARISONS OF RUNTIME AMONG DIFFERENT MBIR METHODS (2D FAN-BEAM, XCAT PHANTOM EXPERIMENTS, AND 12.5% (123) VIEWS)

PWLS-EP ^a	PWLS-DL ^b	PWLS-ST- ℓ_2 ^b	PWLS-ST- ℓ_1 ^c (Alg. 1)
2 minutes	1133 minutes	95 minutes	80 minutes

^aThe PWLS-EP method used 100 iterations with 12 ordered subsets.

^bThe PWLS-DL and PWLS-ST- ℓ_2 methods used 1000 outer iterations.

^cThe PWLS-ST- ℓ_1 method used 1000 outer iterations.

The runtimes were recorded by Matlab implementations on two 2.6 GHz CPUs with 12-core Intel Xeon E5-2690 v3 processors.

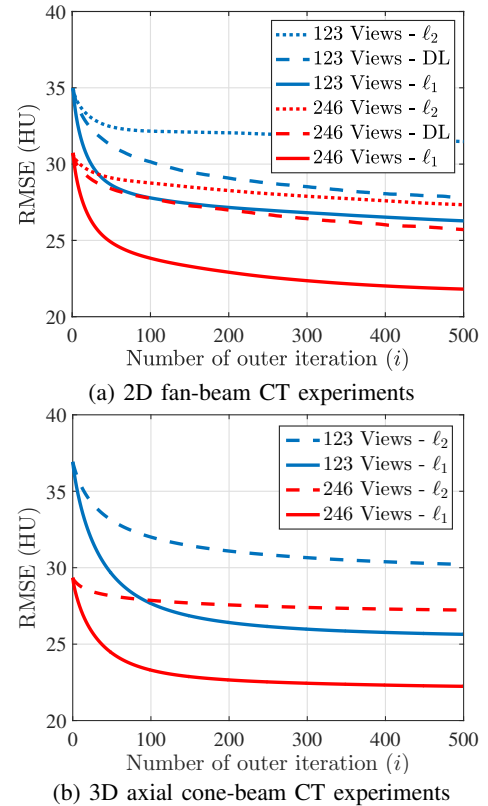


Fig. 5. RMSE convergence behavior for PWLS-ST- ℓ_1 , PWLS-ST- ℓ_2 , and/or PWLS-DL in different CT geometries and projection views.

sparse-view CT reconstructions. To see the effects of using a loose preconditioner in Algorithm 1, we compared the convergence rates of the 3D case with those of 2D (Fig. 5(a) and

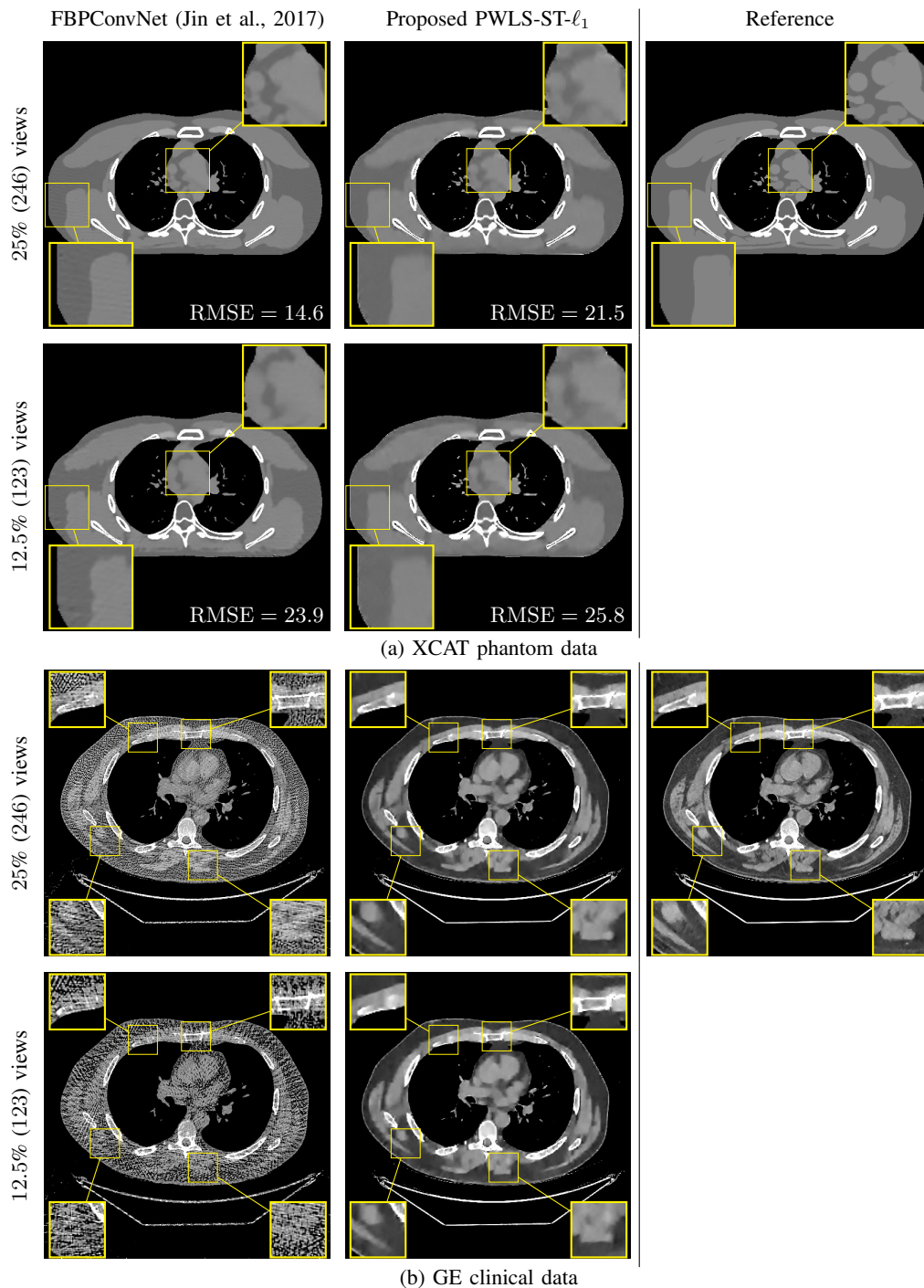


Fig. 6. Generalization capability comparisons between the proposed PWLS-ST- ℓ_1 MBIR method and FBPCConvNet "denoising" method [14] with different number of views (2D fan-beam CT geometry; display window is [800, 1200] HU). For the clinical data, we applied PWLS-EP reconstruction to full-view (984) sinogram to generate the reference image.

Fig. 5(b)). In the first 100 iterations, Algorithm 1 converges faster in 2D experiments than 3D experiments. However, after 100 iterations, the convergence rates of Algorithm 1 are similar in both 2D and 3D reconstructions. In addition, more PCG (with a circulant preconditioner) iterations does not significantly accelerate Algorithm 1 (see Fig 2). These empirically observations imply that, in the 3D sparse-view CT reconstructions, Algorithm 1 using a circulant preconditioner (2 PCG iterations) is a reasonable choice.

3) *Generalization Capability Comparisons between a "Denoising" Deep NN and the Proposed PWLS-ST- ℓ_1 Method:* This section compares the generalization capabilities between the proposed MBIR method, PWLS-ST- ℓ_1 , and a denoising deep NN, FBPCConvNet [14], that are trained from the phantom data; in particular, we tested the trained PWLS-ST- ℓ_1 and FBPCConvNet models to phantom and clinical scan data. The results in Fig. 6 show that the non-MBIR FBPCConvNet method has higher overfitting risks, compared to the proposed PWLS-

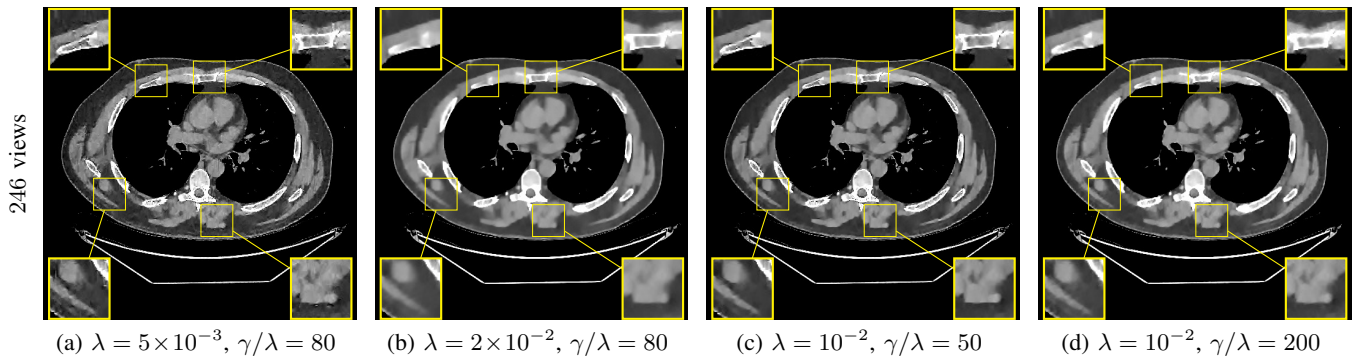


Fig. 7. Comparison of reconstructed images from clinical data for the proposed PWLS-ST- ℓ_1 method with different combinations of regularization parameters λ and γ (2D fan-beam CT geometry; display window is [800, 1200] HU).

ST- ℓ_1 MBIR method. When tested on clinical scan data, PWLS-ST- ℓ_1 achieves much more accurate reconstruction, compared to FBPCovNet. See Fig. 6(b). When tested on phantom data, FBPCovNet generates more unnatural features as the number of views reduces, although it gives lower RMSE values compared to PWLS-ST- ℓ_1 . See zoom-ins in Fig. 6(a). The FBPCovNet results above correspond to those in the recent work [16] that FBPCovNet [14] generated some unexpected structures.

4) *Parameter Selection and Sensitivity of the Proposed PWLS-ST- ℓ_1 Method:* This section describes our parameter selection strategy for PWLS-ST- ℓ_1 reconstruction, and discusses its parameter sensitivity. Our strategy to select its parameters, $\{\lambda, \gamma/\lambda, \kappa_{\text{des},\nu}, \kappa_{\text{des},\mu}\}$, in the XCAT phantom experiments is given as follows. We first chose the hard-shrinkage parameter γ/λ according to the sparsity based guideline described in [36] (specifically, the percentages of non-zero elements in the sparse codes after some outer iterations of Algorithm 1 are 4 – 5%); given chosen γ/λ , we ran a coarse grid search for selecting the regularization parameter λ and the desired condition numbers $\kappa_{\text{des},\nu} = \kappa_{\text{des},\mu}$ in Section II-C4. (In particular, we found that $\kappa_{\text{des},\nu}, \kappa_{\text{des},\mu} \in [10, 50]$ are reasonable for fast and stable convergence of Algorithm 1.)

Our strategy to select the regularization parameter λ for new data, e.g., the GE clinical data in Section III-A1, is given as follows. Given fixed CT geometry, we first compute diagonal majorizers for $\mathbf{A}^T \mathbf{W} \mathbf{A}$ in (P) (see details in [52]) for both the phantom and clinical data, and calculate the mean values of their diagonal elements within a circular ROI. Next, we apply the ratio of these two mean values to the chosen regularization parameter from the phantom experiments, and obtain λ for the clinical data experiments. This procedure aims that the selected λ values give similar regularization strength – particularly across the pixels (or voxels) – to both MBIRs in phantom and clinical data experiments. We found that the other hyperparameters $\{\gamma/\lambda, \kappa_{\text{des},\nu}, \kappa_{\text{des},\mu}\}$ chosen in the phantom experiments work well in the clinical data experiments.

Fig. 7 studies the influence of regularization parameters λ and γ on PWLS-ST- ℓ_1 . Given a fixed hard-shrinkage parameter γ/λ , a larger λ value better removes noise (or unwanted artifacts), but too large λ can oversmooth reconstructed images; compare Fig. 7(a) and Fig. 7(b). Given a fixed regularization parameter λ , a larger γ value leads to lower sparsity in sparse

codes and achieves better noise reduction, but too large γ can remove some edges (e.g., in bone regions); compare Fig. 7(c) and Fig. 7(d). In particular, Fig. S.8 in the supplement shows that once the λ value is properly chosen, PWLS-ST- ℓ_1 is robust to a wide range of γ values.

IV. CONCLUSION

We presented a new MBIR approach for sparse-view CT, PWLS-ST- ℓ_1 that combines PWLS reconstruction and ℓ_1 prior with a learned ST. In addition, we analyzed the empirical MSE for the image update estimator, and the MMSE for the ℓ_2 -norm relaxed image update estimator of the proposed PWLS-ST- ℓ_1 model: the analysis reveals that as the “denoised” sparse codes approach those of the true signal in the learned transform domain, one can obtain better image reconstruction. We introduced an efficient ADMM-based algorithm for the proposed PWLS-ST- ℓ_1 model, with a new ADMM parameter selection scheme based on (approximated) condition numbers. This scheme provided fast and stable convergence in our experiments and helped tuning ADMM parameters of the proposed algorithm for different datasets and different CT imaging geometries.

For sparse-view 2D fan-beam CT and 3D axial cone-beam CT, PWLS-ST- ℓ_1 significantly improves the reconstruction quality compared to conventional methods, such as FBP and PWLS-EP. The comparisons between PWLS-ST- ℓ_1 and the existing PWLS-ST- ℓ_2 model suggest that, model mismatch exists between the training model (1) and the ℓ_2 prior used in PWLS-ST- ℓ_2 . The proposed PWLS-ST- ℓ_1 method using ℓ_1 prior can moderate this model mismatch, and achieved more accurate reconstructions than PWLS-ST- ℓ_2 . Our results with the XCAT phantom data and clinical data show that, for sparse-view 2D fan-beam CT, PWLS-ST- ℓ_1 using a learned *square* ST achieves comparable or better image quality and is much faster compared to the existing PWLS-DL method using learned *overcomplete* dictionary. Our results with clinical data indicate that, deep “denoising” NNs (e.g., FBPCovNet [14]) can have overfitting risks, while MBIR methods trained in an unsupervised way do not suffer from overfitting, and give more stable reconstruction.

Future work will explore PWLS-ST- ℓ_1 with the technique of controlling local spatial resolution or noise in the reconstructed

images [49], [53] to further reduce blur, particularly around the center of reconstructed images (see [41, Appx.] and [36]). On the algorithmic side, to more rapidly solve the block multi-nonconvex problem (P), we plan to apply *block proximal gradient method using majorizer* [24], [26] that guarantees convergence to critical points, or design a more accurate preconditioner that allows the parameter selection scheme in Section II-C4.

APPENDIX A NOTATION

Bold capital letters represent matrices, and bold lowercase letters are used for vectors (all vectors are column vectors). Italic type is used for all letters representing variables, parameters, and elements of matrices and vectors. We use $\|\cdot\|_p$ to denote the ℓ_p -norm and write $\langle \cdot, \cdot \rangle$ for the standard inner product on \mathbb{C}^N . The weighted ℓ_2 -norm with a Hermitian positive definite matrix \mathbf{A} is denoted by $\|\cdot\|_{\mathbf{A}} = \|\mathbf{A}^{1/2}(\cdot)\|_2$. $\|\cdot\|_0$ denotes the ℓ_0 -norm, i.e., the number of nonzeros of a vector. The Frobenius norm of a matrix \mathbf{A} is denoted by $\|\mathbf{A}\|_F$. $(\cdot)^T$, $(\cdot)^H$ indicate the transpose and complex conjugate transpose (Hermitian transpose), respectively. $\text{sign}(\cdot)$ and $\det(\cdot)$ denote the sign function and determinant of a matrix, respectively. For self-adjoint matrices $\mathbf{A}, \mathbf{B} \in \mathbb{C}^{N \times N}$, the notation $\mathbf{B} \preceq \mathbf{A}$ denotes that $\mathbf{A} - \mathbf{B}$ is a positive semi-definite matrix.

ACKNOWLEDGMENTS

The authors thank GE Healthcare for providing the clinical data.

REFERENCES

- [1] G. H. Chen, J. Tang, and S. Leng, "Prior image constrained compressed sensing (PICCS): a method to accurately reconstruct dynamic CT images from highly undersampled projection data sets," *Med. Phys.*, vol. 35, no. 2, pp. 660–663, Feb. 2008.
- [2] I. Y. Chun and T. Talavage, "Efficient compressed sensing statistical X-ray/CT reconstruction from fewer measurements," in *Proc. 12th Intl. Mtg. on Fully 3D Image Recon. in Rad. and Nuc. Med.*, Lake Tahoe, CA, Jun. 2013, pp. 30–33.
- [3] S. Foucart and H. Rauhut, *A mathematical introduction to compressive sensing*. New York, NY: Springer, 2013.
- [4] B. Adcock, A. C. Hansen, and B. Roman, "The quest for optimal sampling: Computationally efficient, structure-exploiting measurements for compressed sensing," in *Compressed Sensing and its Applications*, ser. Applied and Numerical Harmonic Analysis. Birkhuser, Cham, 2015, pp. 143–167.
- [5] I. Y. Chun and B. Adcock, "Compressed sensing and parallel acquisition," *IEEE Trans. Inf. Theory*, vol. 63, no. 7, pp. 1–23, May 2017.
- [6] E. Y. Sidky, C.-M. Kao, and X. Pan, "Accurate image reconstruction from few-views and limited-angle data in divergent-beam CT," *J. X-ray Sci. Technol.*, vol. 14, no. 2, pp. 119–139, 2006.
- [7] H. Yu and G. Wang, "Compressed sensing based interior tomography," *Phys. Med. Biol.*, vol. 54, no. 9, pp. 2791–2805, May 2009.
- [8] J. Bian, J. H. Siewerdsen, X. Han, E. Y. Sidky, J. L. Prince, C. A. Pelizzari, and X. Pan, "Evaluation of sparse-view reconstruction from flat-panel-detector cone-beam CT," *Phys. Med. Biol.*, vol. 55, no. 22, p. 6575, Oct. 2010.
- [9] S. Ramani and J. A. Fessler, "A splitting-based iterative algorithm for accelerated statistical X-ray CT reconstruction," *IEEE Trans. Med. Imag.*, vol. 31, no. 3, pp. 677–688, Mar. 2012.
- [10] S. Niu, Y. Gao, Z. Bian, J. Huang, W. Chen, G. Yu, Z. Liang, and J. Ma, "Sparse-view X-ray CT reconstruction via total generalized variation regularization," *Phys. Med. Biol.*, vol. 59, no. 12, p. 2997, May 2014.
- [11] H. Chen, Y. Zhang, M. K. Kalra, F. Lin, P. Liao, J. Zhou, and G. Wang, "Low-dose CT with a residual encoder-decoder convolutional neural network (RED-CNN)," *IEEE Trans. Med. Imag.*, vol. 36, no. 12, pp. 2524–2535, Jun. 2017.
- [12] E. Kang, J. Min, and J. C. Ye, "A deep convolutional neural network using directional wavelets for low-dose X-ray CT reconstruction," *Med. Phys.*, vol. 44, no. 10, pp. e360–e375, Oct. 2017.
- [13] J. M. Wolterink, T. Leiner, M. A. Viergever, and I. Išgum, "Generative adversarial networks for noise reduction in low-dose CT," *IEEE Trans. Med. Imag.*, vol. 36, no. 12, pp. 2536–2545, May 2017.
- [14] K. H. Jin, M. T. McCann, E. Froustey, and M. Unser, "Deep convolutional neural network for inverse problems in imaging," *IEEE Trans. Image Process.*, vol. 26, no. 9, pp. 4509–4522, Sep. 2017.
- [15] J. Ye, Y. Han, and E. Cha, "Deep convolutional framelets: A general deep learning framework for inverse problems," *SIAM J. Imaging Sci.*, vol. 11, no. 2, pp. 991–1048, Apr. 2018.
- [16] H. Chen, Y. Zhang, W. Zhang, H. Sun, P. Liao, K. He, J. Zhou, and G. Wang, "LEARN: Learned experts' assessment-based reconstruction network for sparse-data CT," *IEEE Trans. Med. Imag.*, vol. 37, no. 6, pp. 1333–1347, Jun. 2018.
- [17] D. Wu, K. Kim, G. E. Fakhri, and Q. Li, "Iterative low-dose CT reconstruction with priors trained by artificial neural network," *IEEE Trans. Med. Imag.*, vol. 36, no. 12, pp. 2479–2486, Dec. 2017.
- [18] I. Y. Chun and J. A. Fessler, "Deep BCD-net using identical encoding-decoding CNN structures for iterative image recovery," in *Proc. IEEE IVMSP Workshop*, Zagori, Greece, Jun. 2018, pp. 1–5.
- [19] I. Y. Chun, H. Lim, Z. Huang, and J. A. Fessler, "Fast and convergent iterative signal recovery using trained convolutional neural networks," in *Proc. Allerton Conf. on Commun., Control, and Comput.*, Allerton, IL, Oct. 2018, pp. 155–159.
- [20] I. Y. Chun, Z. Huang, H. Lim, and J. A. Fessler, "Momentum-Net: Fast and convergent iterative neural network for inverse problems," submitted, Jul. 2019. [Online]. Available: <http://arxiv.org/abs/1907.11818>
- [21] J. Lehtinen, J. Munkberg, J. Hasselgren, S. Laine, T. Karras, M. Aittala, and T. Aila, "Noise2Noise: learning image restoration without clean data," in *Proc. Intl. Conf. Mach. Learn.*, 2018, pp. 2971–2980.
- [22] D. Pelt, K. Batenburg, and J. Sethian, "Improving tomographic reconstruction from limited data using mixed-scale dense convolutional neural networks," *Journal of Imaging*, vol. 4, no. 11, p. 128, 2018.
- [23] N. Yuan, J. Zhou, and J. Qi, "Low-dose CT image denoising without high-dose reference images," in *Proc. 15th Intl. Mtg. on Fully 3D Image Recon. in Rad. and Nuc. Med.*, Philadelphia, United States, Jun. 2019, p. 110721C.
- [24] I. Y. Chun and J. A. Fessler, "Convolutional analysis operator learning: Acceleration and convergence," *IEEE Trans. Im. Proc.* (to appear), Jan. 2019. [Online]. Available: <https://arxiv.org/abs/1802.05584>
- [25] I. Y. Chun, D. Hong, B. Adcock, and J. A. Fessler, "Convolutional analysis operator learning: Dependence on training data," *IEEE Signal Process. Lett.*, vol. 26, no. 8, pp. 1137–1141, Jun. 2019. [Online]. Available: <http://arxiv.org/abs/1902.08267>
- [26] I. Y. Chun and J. A. Fessler, "Convolutional dictionary learning: acceleration and convergence," *IEEE Trans. Im. Proc.*, vol. 27, no. 4, pp. 1697–712, Apr. 2018.
- [27] —, "Convergent convolutional dictionary learning using adaptive contrast enhancement (CDL-ACE): Application of CDL to image denoising," in *Proc. 12th Sampling Theory and Appl. (SampTA)*, Tallinn, Estonia, Jul. 2017, pp. 460–464.
- [28] M. Aharon, M. Elad, and A. Bruckstein, "K-SVD: An algorithm for designing overcomplete dictionaries for sparse representation," *IEEE Trans. Signal Process.*, vol. 54, no. 11, pp. 4311–4322, Nov. 2006.
- [29] J.-F. Cai, H. Ji, Z. Shen, and G.-B. Ye, "Data-driven tight frame construction and image denoising," *Appl. Comput. Harmon. A.*, vol. 37, no. 1, pp. 89–105, Oct. 2014.
- [30] S. Ravishanker and Y. Bresler, " ℓ_0 sparsifying transform learning with efficient optimal updates and convergence guarantees," *IEEE Trans. Signal Process.*, vol. 63, no. 9, pp. 2389–2404, May 2015.
- [31] Q. Xu, H. Yu, X. Mou, L. Zhang, J. Hsieh, and G. Wang, "Low-dose X-ray CT reconstruction via dictionary learning," *IEEE Trans. Med. Imag.*, vol. 31, no. 9, pp. 1682–1697, Sep. 2012.
- [32] L. Pfister and Y. Bresler, "Model-based iterative tomographic reconstruction with adaptive sparsifying transforms," in *Proc. SPIE*, vol. 9020, 2014, pp. 90200H–1–90200H–11.
- [33] C. Zhang, T. Zhang, M. Li, C. Peng, Z. Liu, and J. Zheng, "Low-dose CT reconstruction via L1 dictionary learning regularization using iteratively reweighted least-squares," *Biomed. Eng. OnLine*, vol. 15, no. 1, p. 66, Jun. 2016.

- [34] X. Zheng, Z. Lu, S. Ravishankar, Y. Long, and J. A. Fessler, "Low dose CT image reconstruction with learned sparsifying transform," in *Proc. 2016 IEEE IVMSIP*, Bordeaux, France, Jul. 2016, pp. 1–5.
- [35] X. Zheng, S. Ravishankar, Y. Long, and J. A. Fessler, "Union of learned sparsifying transforms based low-dose 3D CT image reconstruction," in *Proc. 14th Intl. Mtg. on Fully 3D Image Recon. in Rad. and Nuc. Med.*, Xi'an, China, Jun. 2017, pp. 69–72.
- [36] —, "PWLS-ULTRA: An efficient clustering and learning-based approach for low-dose 3D CT image reconstruction," *IEEE Trans. Med. Imag.*, vol. 37, no. 6, pp. 1498–1510, Jun. 2018.
- [37] C. Lu, J. Shi, and J. Jia, "Online robust dictionary learning," in *Proc. 2013 IEEE CVPR*, Portland, OR, Jun. 2013, pp. 415–422.
- [38] W. Jiang, F. Nie, and H. Huang, "Robust dictionary learning with capped ℓ_1 -norm," in *Proc. 2015 IJCAI*, Buenos Aires, Argentina, Jul. 2015, pp. 3590–3596.
- [39] S. Boyd, N. Parikh, E. Chu, B. Peleato, and J. Eckstein, "Distributed optimization and statistical learning via the alternating direction method of multipliers," *Found. & Trends in Machine Learning*, vol. 3, no. 1, pp. 1–122, Jan. 2011.
- [40] W. P. Segars, M. Mahesh, T. J. Beck, E. C. Frey, and B. M. W. Tsui, "Realistic CT simulation using the 4D XCAT phantom," *Med. Phys.*, vol. 35, no. 8, pp. 3800–3808, Jul. 2008.
- [41] I. Y. Chun, X. Zheng, Y. Long, and J. A. Fessler, "Sparse-view X-ray CT reconstruction using ℓ_1 regularization with learned sparsifying transform," in *Proc. 14th Intl. Mtg. on Fully 3D Image Recon. in Rad. and Nuc. Med.*, Xi'an, China, Jun. 2017, pp. 115–119.
- [42] J. B. Thibault, C. A. Bouman, K. D. Sauer, and J. Hsieh, "A recursive filter for noise reduction in statistical iterative tomographic imaging," in *Proc. SPIE 6065, Computational Imaging IV*, vol. 6065, Feb. 2006, p. 60650X.
- [43] I. Y. Chun, B. Adcock, and T. M. Talavage, "Efficient compressed sensing SENSE pMRI reconstruction with joint sparsity promotion," *IEEE Trans. Med. Imag.*, vol. 35, no. 1, pp. 354–368, Jan. 2016.
- [44] J. A. Fessler and S. D. Booth, "Conjugate-gradient preconditioning methods for shift-variant PET image reconstruction," *IEEE Trans. Image Process.*, vol. 8, no. 5, pp. 688–699, May 1999.
- [45] S. D. Booth and J. A. Fessler, "Combined diagonal/Fourier preconditioning methods for image reconstruction in emission tomography," in *Proc. 1995 ICIP*, vol. 2, Washington, DC, Oct. 1995, pp. 441–444.
- [46] L. Fu, Z. Yu, J.-B. Thibault, B. De Man, M. McGaffin G., and J. A. Fessler, "Space-variant channelized preconditioner design for 3D iterative CT reconstruction," in *Proc. 12th Intl. Mtg. on Fully 3D Image Recon. in Rad. and Nuc. Med.*, Lake Tahoe, CA, Jun. 2013, pp. 205–208.
- [47] L. Fu, J. A. Fessler, P. E. Kinahan, and B. De Man, "Combining non-diagonal preconditioning and ordered-subsets for iterative CT reconstruction," in *Proc. 14th Intl. Mtg. on Fully 3D Image Recon. in Rad. and Nuc. Med.*, Xi'an, China, Jun. 2017, pp. 760–766.
- [48] L. A. Feldkamp, L. C. Davis, and J. W. Kress, "Practical cone beam algorithm," *J. Opt. Soc. Am. A*, vol. 1, no. 6, pp. 612–9, Jun. 1984.
- [49] J. H. Cho and J. A. Fessler, "Regularization designs for uniform spatial resolution and noise properties in statistical image reconstruction for 3-D X-ray CT," *IEEE Trans. Med. Imag.*, vol. 2, no. 34, pp. 678–689, Feb. 2015.
- [50] H. Nien and J. A. Fessler, "Relaxed linearized algorithms for faster X-ray CT image reconstruction," *IEEE Trans. Med. Imag.*, vol. 35, no. 4, pp. 1090–1098, Apr. 2016.
- [51] H. Erdoğan and J. A. Fessler, "Ordered subsets algorithms for transmission tomography," *Phys. Med. Biol.*, vol. 44, no. 11, pp. 2835–2851, Nov. 1999.
- [52] I. Y. Chun and J. A. Fessler, "Convolutional analysis operator learning: Application to sparse-view CT," in *Proc. Asilomar Conf. on Signals, Syst., and Comput.*, Pacific Grove, CA, Oct. 2018, pp. 1631–1635.
- [53] J. A. Fessler and W. L. Rogers, "Spatial resolution properties of penalized-likelihood image reconstruction methods: Space-invariant tomographs," *IEEE Trans. Image Process.*, vol. 5, no. 9, pp. 1346–1358, Sep. 1996.
- [54] X. Zheng, I. Y. Chun, Z. Li, Y. Long, and J. A. Fessler, "Sparse-view X-ray CT reconstruction using ℓ_1 prior with learned transform," *IEEE Trans. Computational Imaging*, 2019, *submitted*.

Sparse-View X-Ray CT Reconstruction Using ℓ_1 Prior with Learned Transform – Supplementary Material

This supplement provides additional results to accompany our manuscript [54]. We use the prefix “S” for the numbers in sections, equations, figures, and tables in the supplementary material.

A COMPARISONS OF A DEEP NEURAL NETWORK TRAINED WITH “NOISY” TARGETS AND “CLEAN” TARGETS

Based on the “Noise2Noise” approach [21], we trained a FBPCConvNet [14] network with “noisy” targets by using pairs of FBP-reconstructed images from 123-views and full (984)-views scans. We trained another FBPCConvNet network with “clean” targets by using pairs of FBP-reconstructed images from 123-views scans and ground truth images. See training details in Section III-A2. Fig. S.1 shows image results of FBPCConvNet using noisy targets and clean targets. The image using noisy targets is over-smoothed in bone regions and loses many structural details in lung regions, compared to the one using clean targets. The reason is twofold based on the limitations of the Noise2Noise approach. First, Noise2Noise assumes noise on noisy targets to be zero-mean. However, it is unclear what distributions the artifacts or noise on noisy targets follow. Second, it is difficult to determine which loss function is optimal or reliable for training with noisy targets. This comparison suggests that for methods trained with supervised learning, one would expect improved results by using clean targets in the training processes.

B ADDITIONAL RESULTS

Fig. S.2 shows the FBP reconstructions from the phantom data and the clinical data with 25% (246) projection views and 12.5% (123) projection views.

Fig. S.3 shows an example of the profiles of PWLS-ST- ℓ_1 and PWLS-ST- ℓ_2 . PWLS-ST- ℓ_2 suffers from Gibbs phenomenon due to the model mismatch, and has some ringing artifacts around the edges with high transition.

Fig. S.4 shows the XCAT phantom in the ROI of size $420 \times 420 \times 64$ used for testing in our 3D experiments.

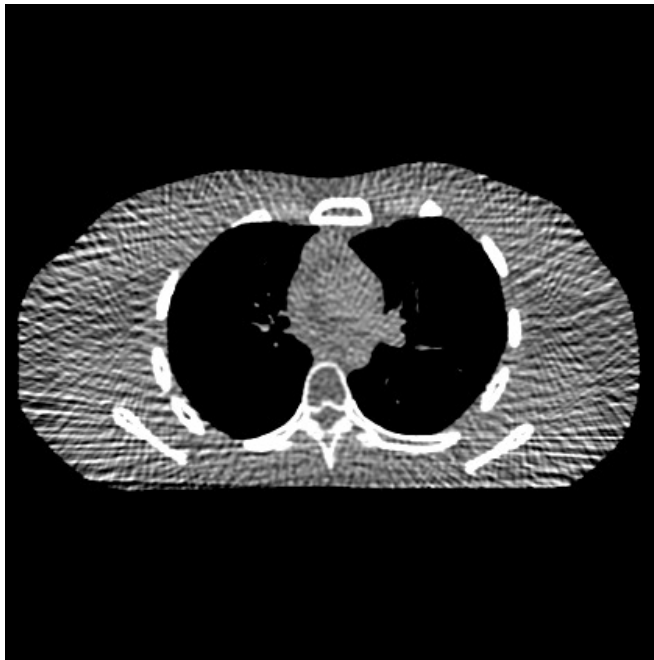
Fig. S.5 shows that the proposed PWLS-ST- ℓ_1 method provides very similar reconstructed images with three different initialization images for both phantom data and clinical data, indicating that PWLS-ST- ℓ_1 is robust to different initializations. (We used the same parameters for the three cases and ran a sufficient large number of iterations (i.e., 5000 iterations) for the case initialized with an image of all ones.) Using a better initialization (e.g., the reconstructed image with PWLS-EP), the proposed PWLS-ST- ℓ_1 method converges faster.

Fig. S.6 shows the error images (corresponding to Fig. 3(a)) of 2D reconstructions with the PWLS-EP, PWLS-DL, PWLS-ST- ℓ_2 , and PWLS-ST- ℓ_1 methods. The proposed PWLS-ST- ℓ_1 approach consistently provides more accurate

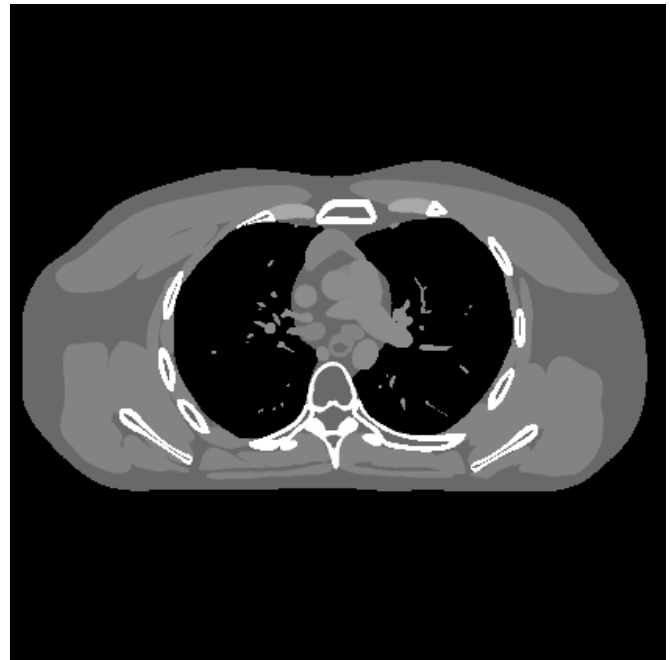
reconstructions compared to the other methods. Specifically, PWLS-ST- ℓ_1 has smaller errors in the heart region (see zoom-ins) of 2D reconstructions than PWLS-ST- ℓ_2 and PWLS-DL. In addition, PWLS-ST- ℓ_1 does not have ringing artifacts around the edges with high transition. Compared to PWLS-ST- ℓ_1 , PWLS-ST- ℓ_2 and PWLS-DL give more and stronger ringing artifacts in reconstruction for 123 views (see zoom-ins).

Fig. S.7 shows the error images (corresponding to Fig. 4) of 3D reconstructed images with the FBP, PWLS-EP, PWLS-ST- ℓ_2 , and PWLS-ST- ℓ_1 methods. The proposed PWLS-ST- ℓ_1 method achieves the lowest RMSE by reducing more noise and reconstructing structural details better, compared to the other methods. In particular, PWLS-ST- ℓ_2 has some ringing artifacts around the edges with high transition for both 123 and 246 views (see zoom-ins).

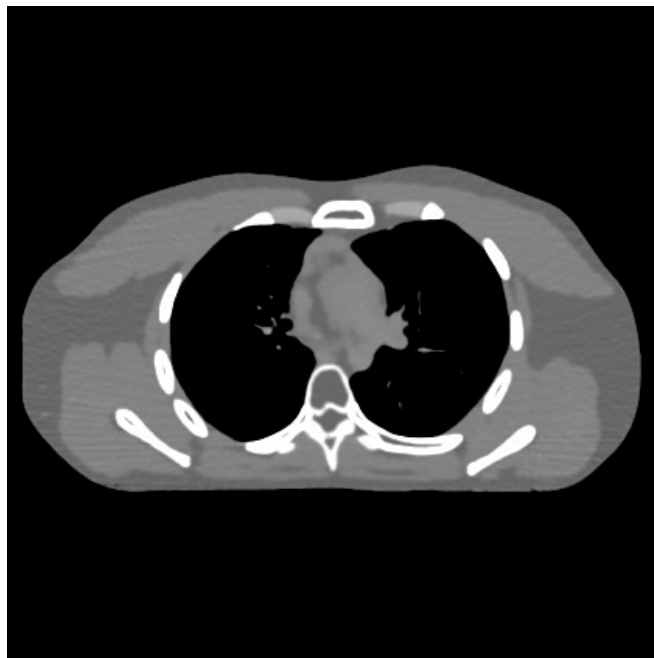
Fig. S.8 shows an additional comparison of 2D reconstructed images from clinical data for the proposed PWLS-ST- ℓ_1 method with 25% (246) views and different γ values. The reconstruction with $\gamma/\lambda = 1000$ is very similar to the one with $\gamma/\lambda = 500$, and only slightly smoother than the one with $\gamma/\lambda = 200$. These results show that in reconstructing the clinical data, once the λ value is properly chosen, PWLS-ST- ℓ_1 is robust to a wide range of γ values.



(a) The input FBP image (123 views)



(b) Ground truth

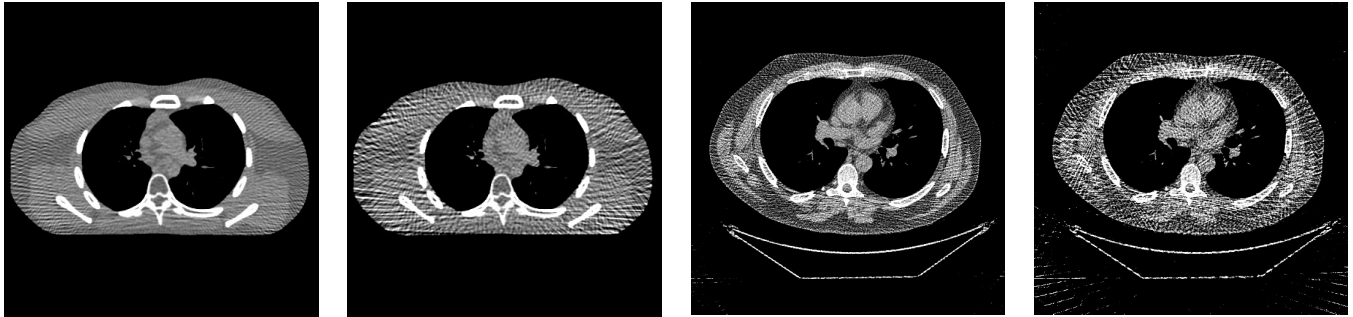


(c) The FBPCConvNet result image using noisy targets



(d) The FBPCConvNet result image using clean targets

Fig. S.1. Comparison of FBPCConvNet result images using noisy targets and clean targets. (a) RMSE = 82.7 HU; (b) RMSE = 54.8 HU; (c) RMSE = 23.9 HU. Display window is [800, 1200] HU.



(a) Phantom data, 25% (246) views (b) Phantom data, 12.5% (123) views (c) Clinical data, 25% (246) views (d) Clinical data, 12.5% (123) views

Fig. S.2. The FBP reconstructions from the phantom data and the clinical data with different number of views. Display window is [800, 1200] HU.

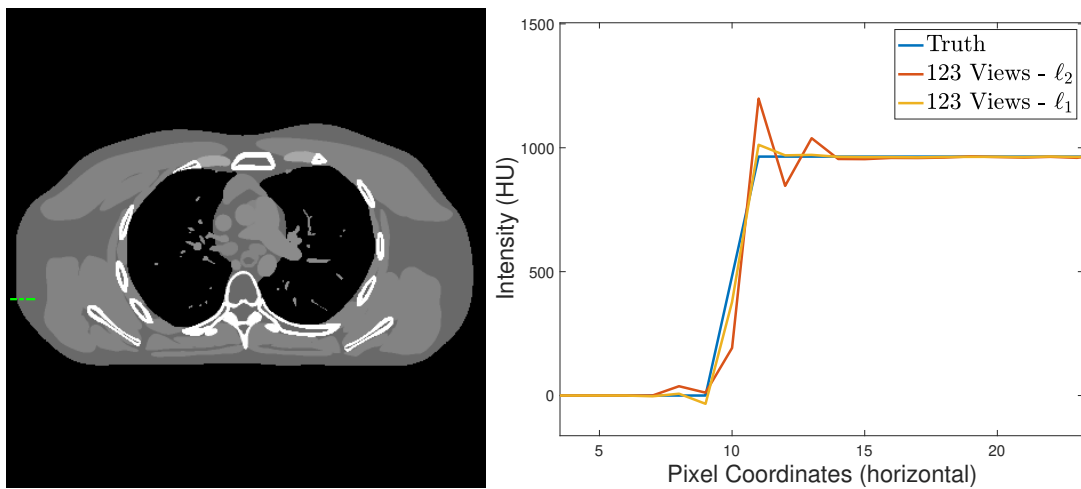


Fig. S.3. Profile of XCAT reconstructions for the PWLS-ST- ℓ_2 and PWLS-ST- ℓ_1 methods (2D fan-beam and 123 views). The profile location is indicated by a green line.

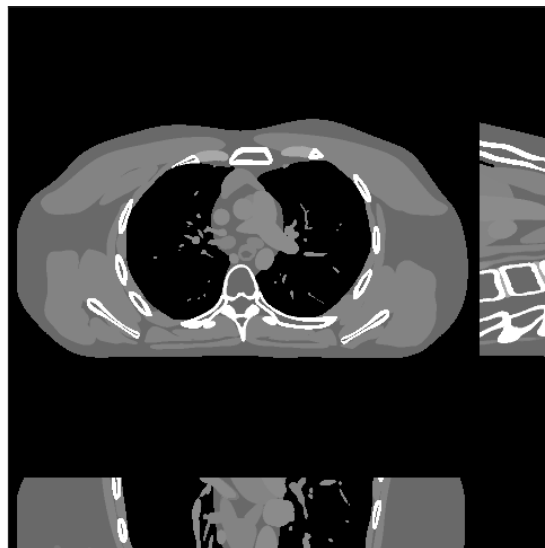


Fig. S.4. The XCAT phantom in the ROI of size $420 \times 420 \times 64$ used for testing in our 3D experiments. Display window is [800, 1200] HU.

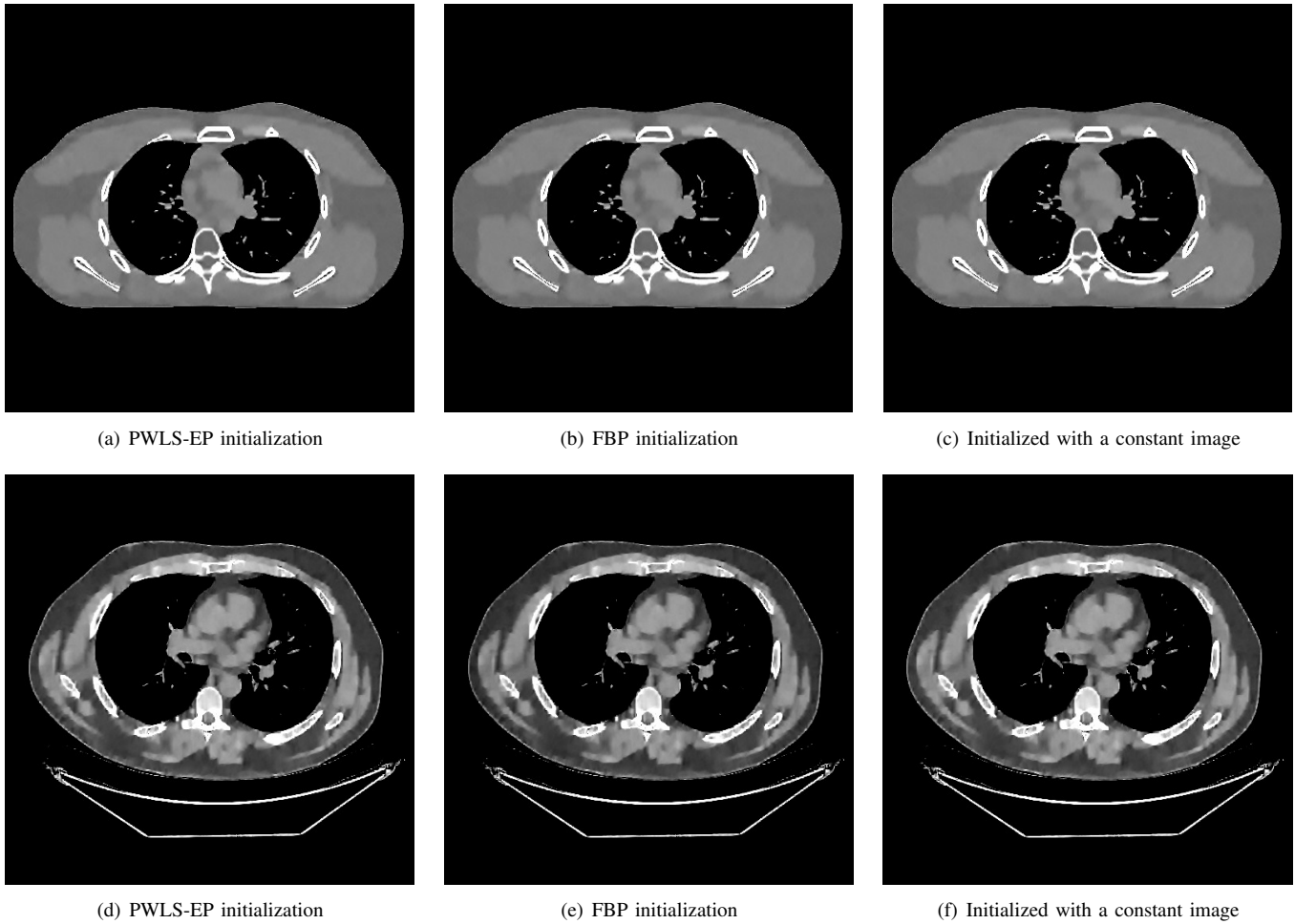


Fig. S.5. Comparison of 2D reconstructed images from phantom data (first row) and clinical data (second row) for the proposed PWLS-ST- ℓ_1 method with different initializations. (2D fan-beam CT geometry with 123 views; display window is [800, 1200] HU). (a) RMSE = 25.8 HU; (b) RMSE = 25.9 HU; (c) RMSE = 26.3 HU.

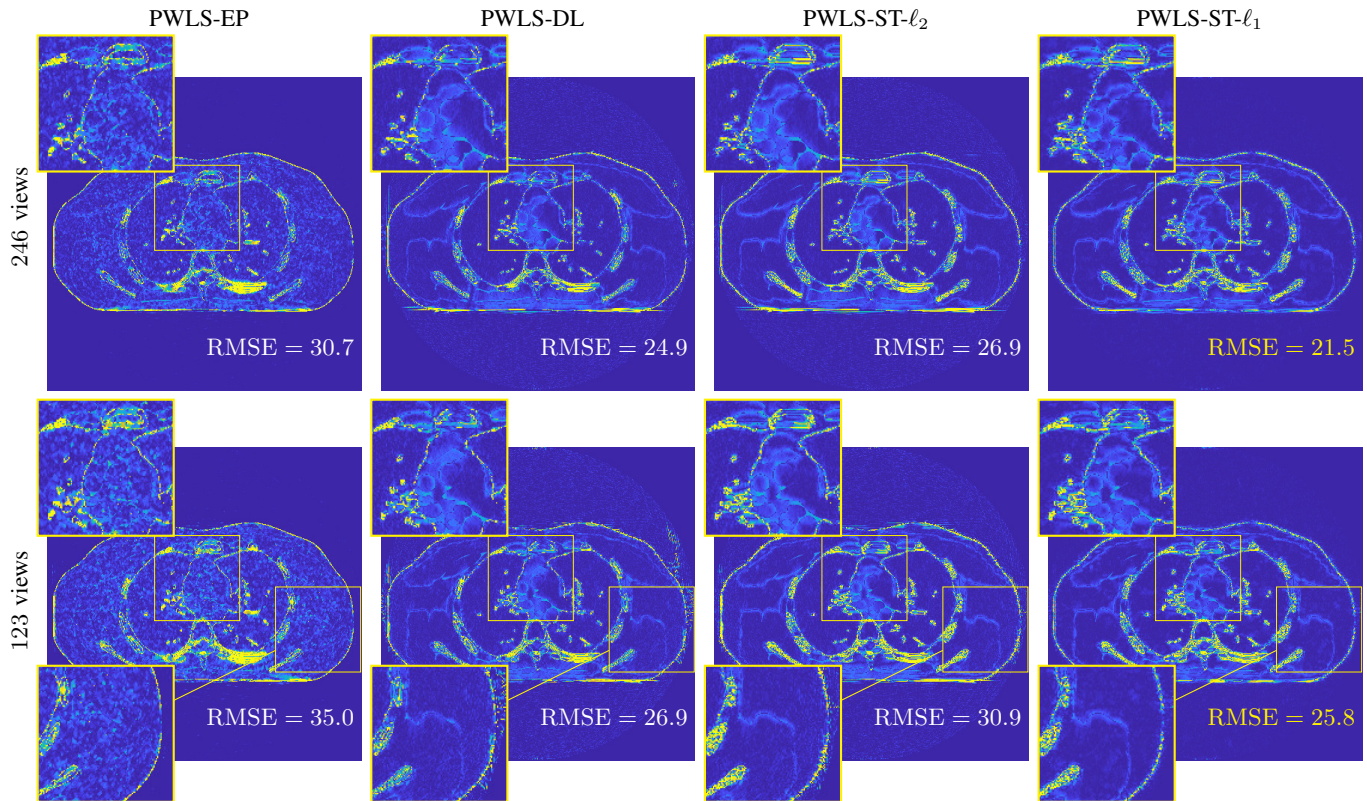


Fig. S.6. Corresponding error images of 2D reconstructed images from different X-ray CT reconstruction models with different number of views (2D fan-beam CT geometry and $\rho_0 = 10^5$). Display window is $[0, 100]$ HU.

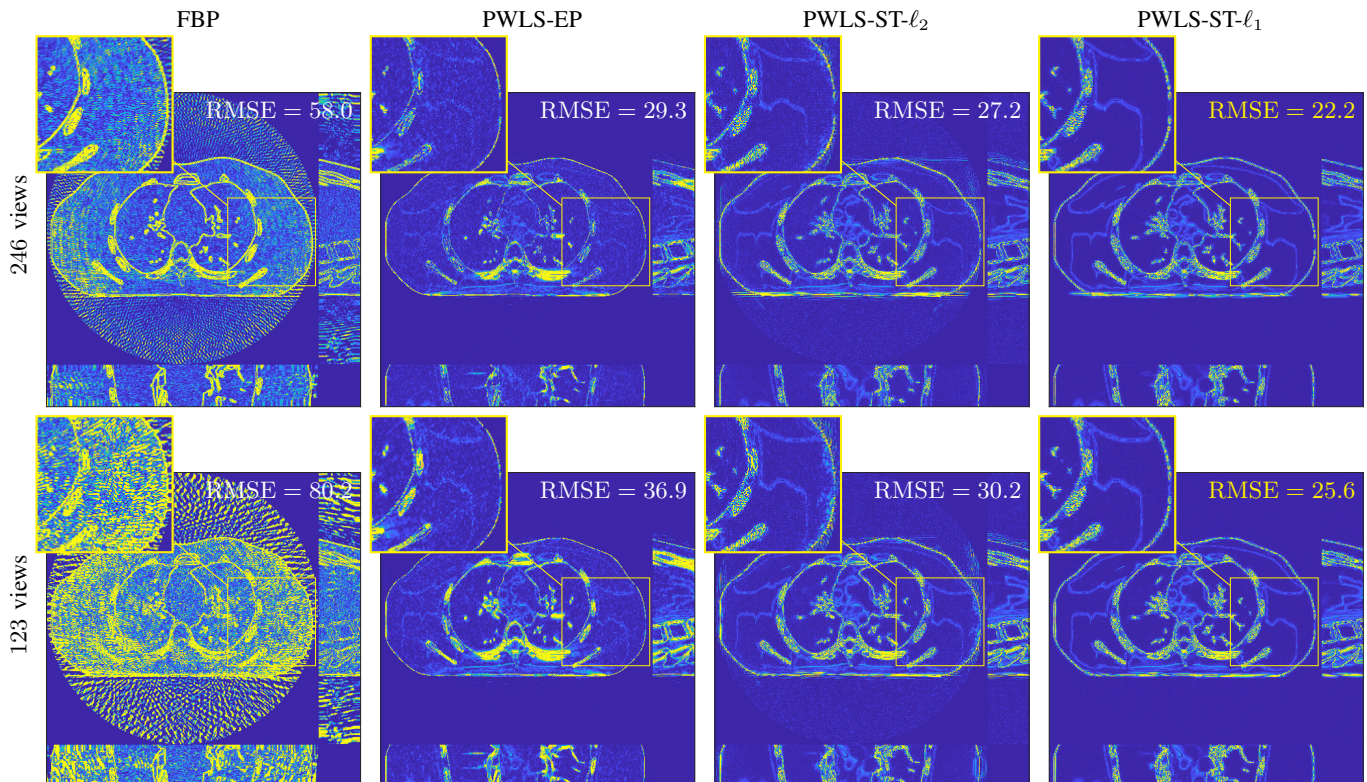


Fig. S.7. Corresponding error images of 3D reconstructed images from different X-ray CT reconstruction models with different number of views (axial 3D cone-beam geometry and $\rho_0 = 10^5$; display window is $[0, 100]$ HU; displayed for the central axial, sagittal, and coronal planes).

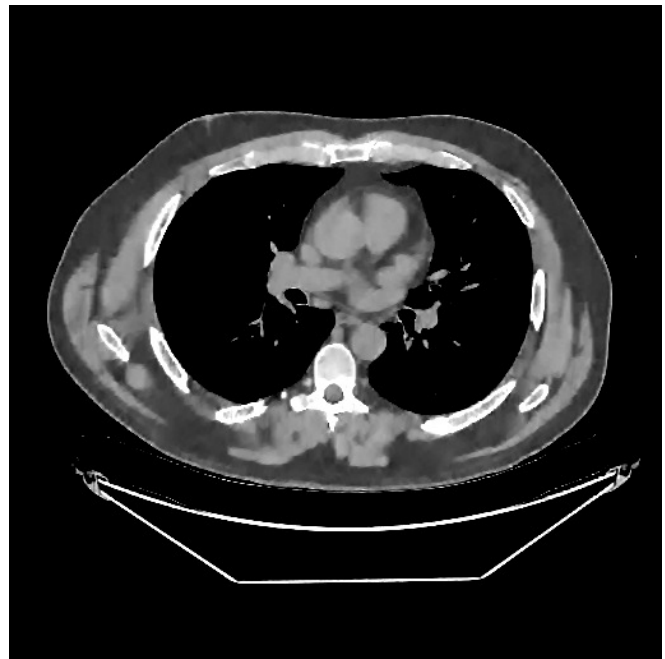
(a) $\lambda = 10^{-2}, \gamma/\lambda = 50$ (b) $\lambda = 10^{-2}, \gamma/\lambda = 200$ (c) $\lambda = 10^{-2}, \gamma/\lambda = 500$ (d) $\lambda = 10^{-2}, \gamma/\lambda = 1000$

Fig. S.8. Comparison of 2D reconstructed images from clinical data for the proposed PWLS-ST- ℓ_1 method with 25% (246) views and different γ values. Display window is [800, 1200] HU.